Defect-Driven Reactivity of Layered Materials Examined through Atomic Layer Deposition

Thesis by

Michael Francis Mazza

In Partial Fulfillment of the Requirements for the Degree of

Doctor of Philosophy

CALIFORNIA INSTITUTE OF TECHNOLOGY
Pasadena, CA

2022
(Defended August 25, 2021)

Michael Francis Mazza
ORCID: 0000-0003-3995-3100

ACKNOWLEDGEMENTS

No one ever does anything alone, no matter what lies we tell ourselves. The work detailed in this thesis is attributed to me, though every colleague, friend, and mentor I have had during my scientific career shares credit for this work. I will make no excuses for forgetting people here.

First and foremost I would like to thank my advisor Nate Lewis for bringing me into his lab on my first day at Caltech. He puts immense effort into cultivating a lab-as-community where students take on an active role in mentoring one another and directing their own projects. The surface chemistry described in this thesis would have been shut down if he and other members of the group didn't encourage me at every step. He fosters an environment where science is collaborative and exciting and for that I will always be grateful.

My committee members, Kimberly See and Jack Beauchamp, have been extremely supportive during my time at Caltech. You encouraged me to take risks with my work and your feedback has been immensely helpful these past 5 years. Bruce Brunschwig deserves special recognition, as some of my fondest memories of research at Caltech have revolved around maintaining and troubleshooting the X-ray photoelectron spectrometers in his lab. Whether I spent half a day soaked in water spilling from a pump and vowed to wear a bathing suit next time, or the instant regret I felt after I attempted to siphon the cooler water with my mouth, there wasn't a dull moment.

Barbara Miralles and Kimberly Papadantonakis have always been extremely helpful, organized administrators that kept me on track and always looked for ways to help. Barbara, you were extremely helpful and supportive during Noyes-specific issues such as the now-biblical flood and the long-fought battle to rid the lab of dust. Kimberly, you have offered great professional advice and I am so grateful to call you a friend and colleague.

My undergraduate advisor, Sophia Hayes, took a chance on a sophomore student who only knew that he hated organic chemistry and had no idea what he wanted to do. I couldn't imagine making a decision like that, but working in her lab taught me how to be a good scientist and set me on this track. I am also grateful for Michael West, a graduate student in her lab, who I still call a great friend.

Noah and Josh left only a few short months after I joined the Lewis Group, but they paved the way for the surfaces and 2D materials work that became my thesis. Fadl, Dan, Lichterman, and Stefan acted as my elders, and I regret not listening to you all more, though I always enjoyed your company and perspective. Miguel Cában-Acevedo deserves special recognition, as we spent many days and evenings in the BI talking about the work that became this thesis, struggling to figure out the science, but always moving forward. You were a great mentor and colleague, and I regret that we became closer friends just as you were leaving. Burt Simpson and Annelise Thompson were excellent mentors and were extremely patient with my questions, pestering, and general well-defined antics.

My officemates Ethan, Jonathan, Ellen, and Mo helped make Noyes the special place that it is. Never a dull moment, as they were always eager (or sometimes over-eager) to help and talk. You all kept me smiling, laughing, and excited to go to work each day. Azhar Carim also deserves special recognition, for constantly pushing me to ask better questions about my science. Of course, also for being the most effective Devil on my Shoulder and a good friend.

I want to recognize the many friends and familiar faces in the Lewis Group. Paul K, Paul N, Kat, Weilai, Harold, Katie, Jackie, Sean, and Alex. From the softball field to the Anza-Borrego desert, I am privileged to call you friends and colleagues. Zach, Elizabeth, Jake, Madeline, and Christian have been extremely supportive and I am lucky to count you all as dear friends.

My time at Caltech would have been incomplete without the CTLO. Kitty Cahalan and Mitch Aiken are inspirational for their dedication to teaching and outreach, and they make Caltech and Pasadena a better place for it. The Visiting Scientists program is the longest-running project of my Ph.D. We started it in January 2017, and I did not start the work that became this thesis until spring 2017. I am extremely proud of the program and am indebted to the hard work and dedication of Cecilia Sanders, Kevin Barraza, Hannah Allen, Keefe Mitman, Anushri Dixit, and Inha Cho for the incredible success of this program.

To my Caltech friends, Cora, Emily, Sara, Natalie, and Chris, thank you for all the great times and the support these past few years. To non-Caltech friends, Chris, Frost, Emily, Brittney, Madison, AC, and Jack, thank you for accompanying me on this crazy ride.

To my family, thank you for your constant support, love, and validation. All of you have been a refuge during the most difficult periods of the past 5 years, and this accomplishment is yours as much as it is mine. To Thomas and Genevieve, thank you for being the best brother and sister I could ask for. You are always dependable, supporting and caring when I need it most.

To Haley, for whom words escape me. The impact you have had on my life is immeasurable. You have been with me every step of the way, offering nothing but support, love, and encouragement. Your talent, intellect, and humor brighten every day, and I am so grateful for the life we have together. Thank you, simply, for filling my life with joy.

ABSTRACT

Layered materials are a unique class of materials that are characterized by strong covalent bonds in single layers in the two-dimensional plane, but much weaker van der Waals interactions between layers. This unique bonding environment gives rise to remarkable chemical and physical properties. These materials can be easily exfoliated into single atomic layers, true two-dimensional materials, or few-layer stacks. As the number of layers changes, the physical and chemical properties can be modified. Similarly, as the relative position of one or more layers is changed, this change in the bonding environment has substantial impacts on the properties. Due to their unique bonding environment, layered materials are unusually inert to atomic layer deposition. Atomic layer deposition (ALD) is a surface-sensitive deposition technique that relies on a sequence of chemical reactions on the surface of a substrate to deposit the target material. Using this surface-sensitive deposition technique, the crystal structure and chemical bonding environment of the layered material can be interrogated.

Chapter 1 investigates the spontaneous formation of highly ordered triangular and linear pattern depositions on layered material substrates. These patterns form with two different layered material substrates and with two separate ALD reactions. The pattern depositions do not change with increasing deposition time or with different concentrations of reactants. These networks, while highly unusual to observe chemically, are discussed through a well-established dislocation theory, where defects in the crystal structure of layered materials can impact the surface reactivity.

Chapter 2 explores the stacking order characteristics of few-layer materials and discusses how changing the stacking order can change the crystal structure and the

electronic properties of the materials. The chapter describes the field of few-layer materials and the process of modifying or transferring nanoflakes to new substrates. The chapter introduces a new transfer system that allows for patterned nanoflakes with stacking fault networks to be transferred to new substrates with micron-scale precision. The crystal structure of both the deposited triangular networks and the layered material beneath is discussed.

Chapter 3 describes a new approach to selectively target defect sites in monolayer graphene. A new, water-free atomic layer deposition chemistry is introduced to precisely react metal oxides with high-energy defect sites on graphene. The quality of the film is interrogated, and the selectivity of the film is determined by measuring the thickness of the film deposited on the defect-rich regions. The results confirm that this ALD process creates a robust passivating film while keeping the unperturbed regions clean of any metal oxide.

PUBLISHED CONTENT AND CONTRIBUTIONS

Mazza, M. F.; Cabán-Acevedo, M.; Wiensch, J. D.; Thompson, A. C.; Lewis, N. S. Defect-Seeded Atomic Layer Deposition of Metal Oxides on the Basal Plane of 2D Layered Materials. *Nano Lett.* **2020**, *20* (4), 2632–2638. https://doi.org/10.1021/acs.nanolett.0c00179.

> M.F.M. co-designed the project, performed all experiments except for TEM, collected and prepared the data, and co-wrote the manuscript with M.C.A.

Mazza, M.F.; Cában-Acevedo M.C.; Fu, H.J.; Meier, M.C.; Thompson, A.C.; Ifkovits, Z.P.; Carim, A.I.; Lewis, N.S. Selective-Area, Water-Free Atomic Layer Deposition of Metal Oxides on Graphene Defects. *ACS Materials Au* **2021**

> M.F.M. co-designed the project, collected the data, and wrote the manuscript.

Table of Contents

List of Figures and Data

Chapter 1

Defect-Driven Atomic Layer Deposition of Metal Oxides on 2D Layered Materials

Adapted from:

Mazza, M. F.; Cabán-Acevedo, M.; Wiensch, J. D.; Thompson, A. C.; Lewis, N. S. Defect-Seeded Atomic Layer Deposition of Metal Oxides on the Basal Plane of 2D Layered Materials. *Nano Lett.* **2020**, *20* (4), 2632–2638. https://doi.org/10.1021/acs.nanolett.0c00179.

1.1 Introduction

2D layered materials, such as graphite and transition metal dichalcogenides (MX_2, where M = Mo and W, and X = S, Se, and Te), have strong, covalent in-plane bonding and weak van der Waals interactions between layers. Within the few-layer to monolayer regime, the electronic, chemical, and optical properties of layered materials are dependent on thickness, stacking order, and relative stacking orientation.[1-3] Given the variety of electronic structures and chemistry of 2D materials, and their tunability at the nanoscale, this class of materials has been actively investigated in applications such as catalysis,[4,5] batteries,[6,7] and photovoltaics.[8,9]

Pristine basal surfaces on bulk 2D single crystals and/or pristine few-layer stacks of 2D materials commonly used in application-focused studies are generally prepared by mechanical exfoliation with adhesive tape. Transmission electron microscopy (TEM) studies have shown that mechanical exfoliation can disrupt the relative stacking orientation of 2D layers at or within a few layers of the surface of the single crystal.[10] The disruptions caused by the shear and twist forces involved in the mechanical exfoliation process can induce surface corrugation and can also form dislocation networks near the surface and along the basal plane. Mechanical exfoliation can consequently induce defect patterns and networks that modify the local electronic structure and chemical reactivity of the basal plane surface.[11-13]

In principle, the local differences in properties induced by defects can consequently alter the chemical reactivity of the surface. Such heterogeneity can be exploited to produce patterned deposition using defect-selective deposition methods and reaction conditions. Atomic layer deposition (ALD) allows excellent thickness control and film conformity, and consequently is used to fabricate gate dielectrics as well as protective coatings for photoelectrochemical devices.[14,15] ALD utilizes sequential, self-limiting chemical reactions for the controlled growth of highly conformal films on the surface of a target substrate. Selective-area ALD has been demonstrated by use of an assisting self-absorbed monolayer to inhibit facile penetration of precursor molecules through the monolayer to the surface of the substrate.[16] Selective ALD has also been reported at boundaries and step edges on the basal plane surface of 2D layered materials.[17,18] While such studies exploit the high-reactivity of dangling bond and grain boundary defect sites to achieve preferential deposition, an alternative approach would exploit the surface energy landscape introduced by defect networks originating solely from disruption of van der Waals (non-bonding) interactions to produce patterned deposition.

In this chapter, we report the spontaneous, unassisted growth of highly ordered triangular arrays of metal oxide particles on the basal surface of mechanically exfoliated molybdenum disulfide (MoS_2) as well as on the basal plane of highly oriented pyrolytic graphite (HOPG). The ALD reaction conditions and the metal organic precursor were systematically studied to understand the origin and generality of the patterned deposition.

Additionally, the presence of dislocation networks prior to deposition was investigated by TEM.

1.2 Deposition Conditions, Materials, and Methods

Naturally occurring molybdenum disulfide (MoS_2) was purchased from 2D Semiconductors as well as from SPI supplies. Highly ordered pyrolytic graphite (HOPG) was purchased from SPI Supplies. Prior to deposition, samples were exfoliated multiple times with scotch tape (3M Company) or blue tape (Nitto Denko) to expose a pristine, flat surface. No difference in deposition patterning was observed resulting from use of different types of tape.

Titanium dioxide (TiO_2) and manganese oxide (MnO_x) were deposited using a Cambridge Nanotech S200 ALD system. All depositions were performed with 20 sccm of N_2 carrier gas at 150˚C at a base pressure of ~ 0.8 Torr. Tetrakis(dimethylamido)titanium (IV) (TDMAT, 99.999% Sigma Aldrich) heated to 75 ˚C was used as the titanium precursor. 18.2 MΩ resistivity (Millipore) water at room temperature was used as the counter reactant. MnO_x was deposited from bis(ethylcyclopentadienyl)manganese ($(EtCp)_2Mn$ 98% STREM) heated to 95 ˚C.

Exfoliated crystals were placed directly into the ALD chamber on top of a small glass microscope slide. After each deposition, spectroscopic ellipsometry was performed on the glass slide with an absorbing oxide model. This approach yielded film thicknesses and ALD growth rates in general agreement with expected literature values and was confirmed with atomic force microscopy (AFM). The data shown in Figures 1-1, 1-2, and

1-4 used the following ALD recipe given in Equation 1. For Figure 1-3, the same recipe is used, but the TDMAT pulse time is varied.

$$0.015\ \text{s}(H_2O) – 15\ \text{s} – 0.1\text{s}(\text{TDMAT}) – 20\ \text{s} \qquad (1)$$

This recipe indicates a pulse time of 0.015 s for H_2O, followed by a 15 s purge time to remove unreacted precursors. This is followed by a 0.1 s pulse of TDMAT and a 20 s purge time.

Atomic force micrographs were collected using a Bruker Multimode 8 Atomic Force Microscope in air. Scans were collected in ScanAsyst mode using SiN tips with a nominal spring constant of 0.4 N m^{-1}. Scanning electron microscopy (SEM) was performed using a FEI Nova NanoSE 450 at accelerating voltages of 3 and 5 keV with a 5 mm working distance.

Multilayer MoS_2 TEM samples were prepared by mechanical exfoliation of commercial bulk single crystals using blue tape (Nitto Denko) followed by gentle dry transfer of the exfoliated flakes onto a TEM grid (C-Flat Holey Carbon 1.2/1.3um 200 mesh copper grid from Electron Microscopy Sciences). Transmission electron microscopy (TEM) data were collected using a FEI Tecnai Polara (F30) TEM at an accelerating voltage of 200 keV.

1.3 Effect of ALD conditions on Pattern Formation

After deposition, the deposited film undergoes a color change from silver to yellow at thicknesses between 10-40 nm. Between 40-70 nm, the TiO_2 film is a bright purple, and beyond approximately 70 nm, the film turns blue. These film colors provide optical contrast between the bare crystal surface and the patterned film. This pattern is shown in the scanning electron microscopy (SEM), AFM, and optical microscopy images shown in Figure 1-1.

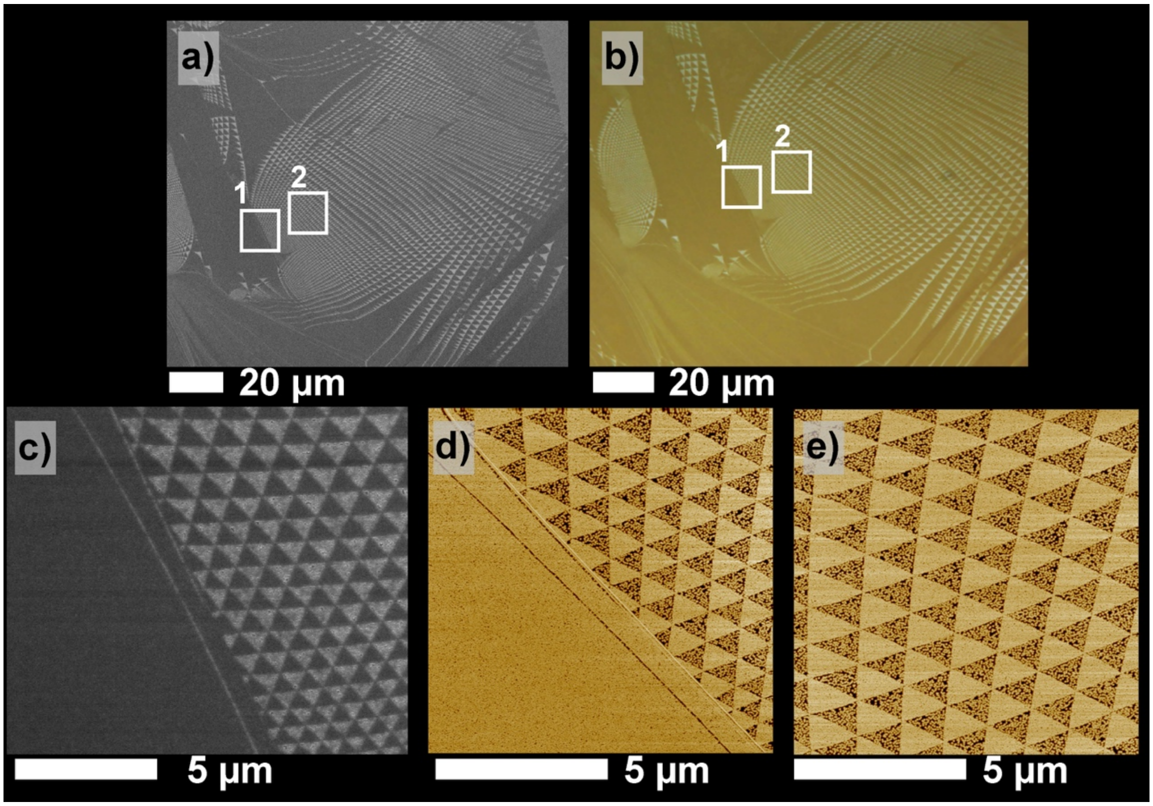

Figure 1-1. SEM image of highly ordered patterned area on MoS_2 after 800 cycles of TDMAT and H_2O (a). Optical microscope image of the same area (b). Close up SEM image of the region indicated in box 1 (c). Close up AFM image of the same region indicated in box 1(d). AFM image of the highly ordered patterned region in box 2(e).

As shown in Figure 1-1, the thin yellow film indicates regions where TiO_2 has deposited, with the bright regions showing the bare MoS_2 substrate and a loose assembly of nanoparticles. High-resolution AFM and SEM of the same region (Figures 1c and 1d) illustrate that the electron microscopy contrast directly matches the topographic profile.

Figure 1-2 shows a separate sample at a different supersaturation condition after 1000 ALD cycles and a line trace showing the height profile. The height profile indicates a film thickness of approximately 53 nm, giving an approximate ALD growth rate of 0.5 Å cycle^{-1}. This is in good agreement with reported literature values at 150 ˚C.[19] Ellipsometric data on the same sample is also in good agreement, yielding a film thickness of 55 nm. Given the data shown in these two figures, it is clear that there exists two distinct triangular regions; one where deposition occurs readily and the other where the bare substrate is exposed with minimal nanoparticle aggregation in the interior.

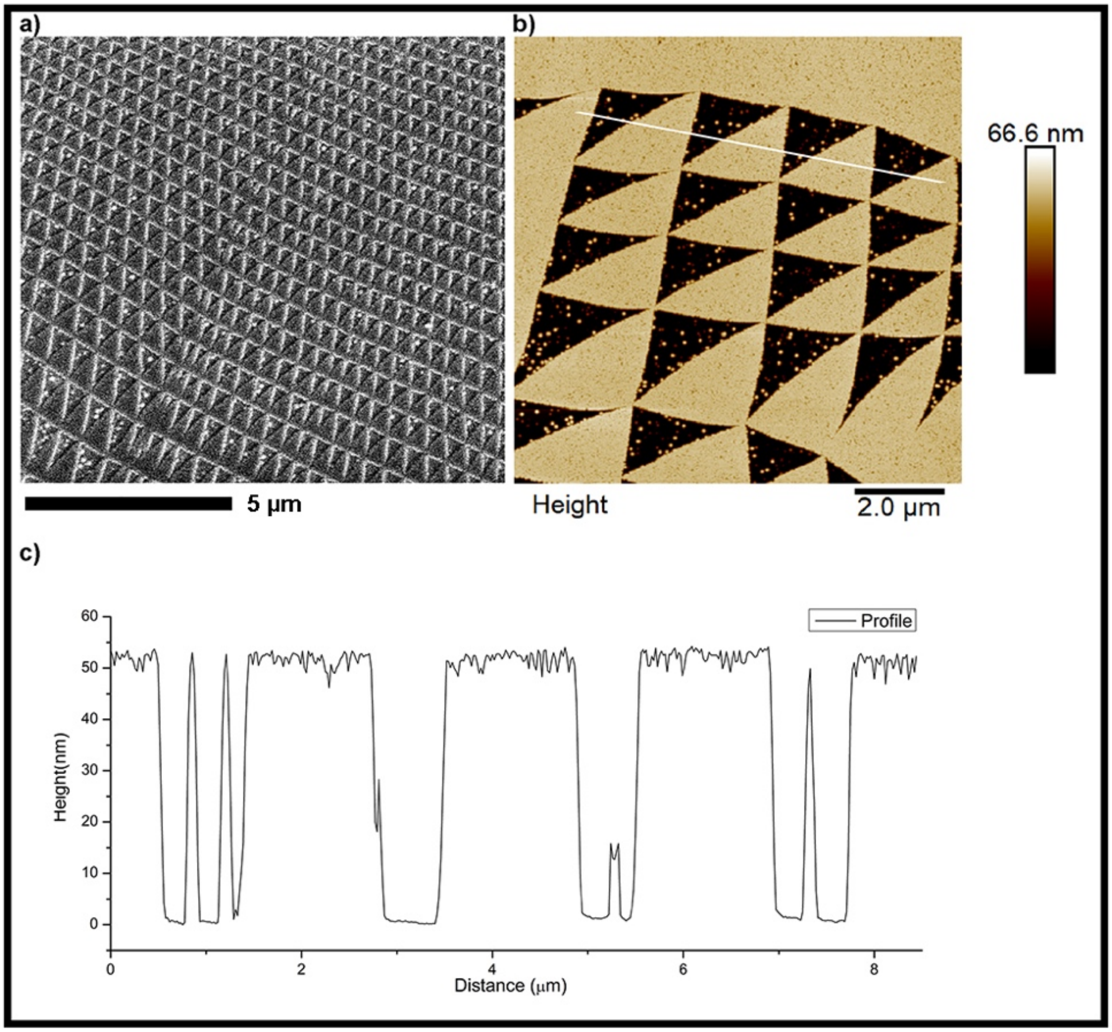

Figure 1-2. SEM image of a highly ordered, patterned area on exfoliated MoS_2 after 1000 cycles of TiO_2 (a). AFM image of a different region on the same sample (b). Height profile of the AFM image across the white line (c).

To investigate this unique growth behavior, MoS_2 crystals were exposed to different concentrations of TDMAT. Figure 1-3a-f shows SEM images for three mechanically exfoliated MoS_2 crystals covered with 1000 ALD cycles of TiO_2. The TiO_2 was formed using different TDMAT precursor dose times, *t*(TDMAT), while using water as the counter reactant. For *t*(TDMAT) = 0.025 s, in certain regions of the basal surface, the TiO_2 film formed a highly ordered network consisting of triangularly shaped island deposits that shared corners and overall orientation. Very little nanoparticle deposition was observed in the interior of the opposite-facing triangularly shaped empty spaces generated by the TiO_2 film pattern (Figure 1-3d).

The dose time for the metal organic precursor was then systematically increased to investigate the effect that TDMAT concentration per cycle in the ALD chamber had on the TiO_2 film growth and on the morphology of the network pattern. Increases in the dose time produced a concomitant increase in the TiO_2 film growth-per-cycle (GPC). Ellipsometry data indicated a GPC of 0.47 Å cycle^{-1}, 0.55 Å cycle^{-1}, and 0.73 Å cycle^{-1} for dose times of 0.025 s, 0.1 s, and 0.4 s, respectively. The ellipsometry data of the GPC values were in accord with TiO_2 film-thickness data determined using atomic-force microscopy shown in Figure 1-2. As the dose time was increased to *t*(TDMAT) = 0.1 s, the concentration of nanoparticles within the opposite-facing triangularly shaped empty spaces gradually increased. The smoothness and uniformity of the triangularly shaped TiO_2 deposition also improved, indicating an increase in the conformality and compactness of the TiO_2 film. At *t*(TDMAT) = 0.4 s, the empty spaces were mostly filled with TiO_2 nanoparticles. Moreover, these opposite-facing triangularly shaped regions displayed a brighter contrast under SEM, due to the decrease in the conformality and compactness of the film in these regions.

The dose time data clearly indicates the emergence of inert, triangular regions on selected areas of the basal plane surface through a range of ALD reaction conditions. Assuming inhomogeneous surface reactivity, at short dose times the low TDMAT concentration shifts the reaction towards a lower supersaturation, more selective condition, and the TiO_2 deposition becomes favorable only on the most reactive (high-energy) basal surface sites. In contrast, at longer dose times, and correspondingly high growth rates, the increase in the TDMAT concentration shifts the reaction towards a higher supersaturation condition, with deposition of TiO_2 resulting in a conformal film outside of these bright triangular regions. The reported linear growth rate for TDMAT and H_2O at 150 ˚C is ~ 0.52 Å $cycle^{-1}$.[19] The growth rate at the longest dose time is 50% higher than expected, so the random nanoparticle deposition in the empty spaces could indicate fractional CVD-type deposition, which correspondingly increases as the precursor dose time increases. The observed film patterns therefore suggest that the basal surface contains areas where the surface energy is organized in a network pattern comprising a continuous array of two distinct opposite-facing triangularly shaped regions with substantially different reactivities.

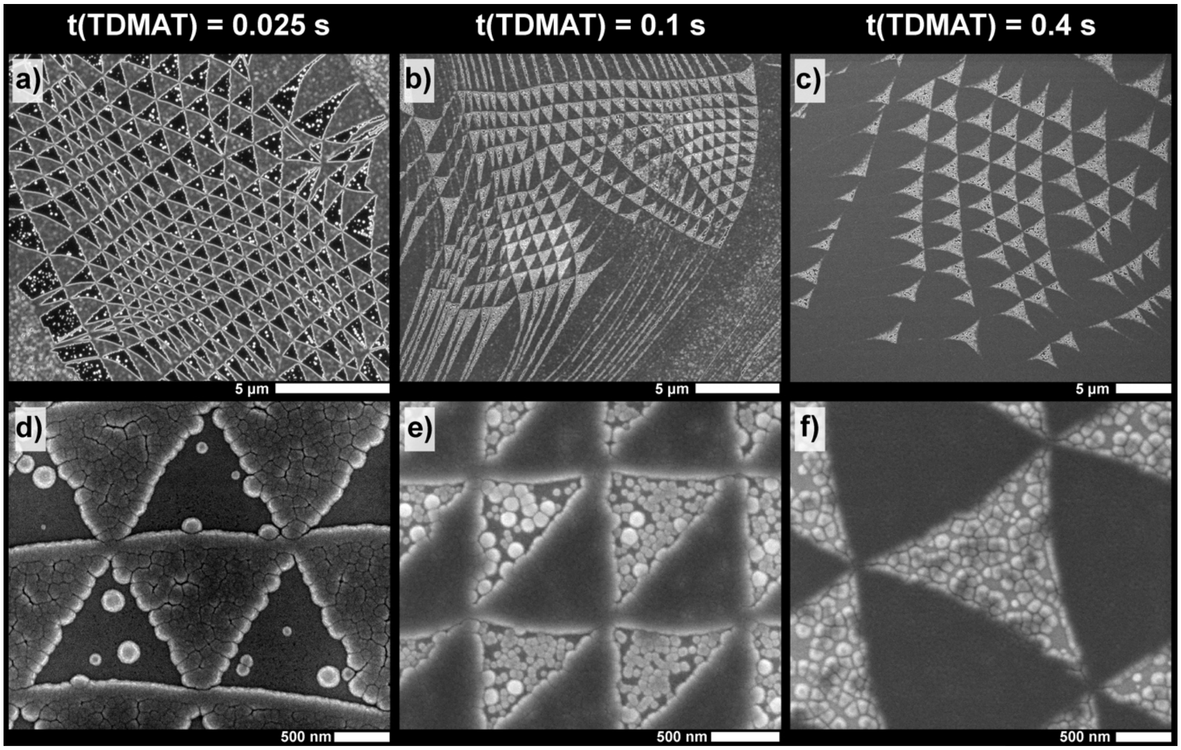

Figure 1-3. SEM images of patterned regions on MoS_2 after 1000 ALD cycles of TDMAT and H_2O when the pulse time of TDMAT was varied from (a,d) 0.025 s, (b,e) 0.1 s, and (c,f) 0.4 s, respectively. Scale bars are 5 μm (a,b,c) and 500 nm (d,e,f).

The development of the highly ordered triangular networks as a function of film thickness was interrogated by monitoring the same patterned region with an increasing number of cycles. Figure 1-4 shows the evolution of the morphology of the TiO_2 film pattern as the deposition proceeded through 200, 400, and 1000 cycles, respectively, on exfoliated MoS_2 with a dose time of t(TDMAT) = 0.1 s. These depositions were performed in a laminar flow ALD chamber, where precursors are introduced on one end of the chamber and travel laterally across the chamber towards the outlet with the pump. These systems can lead to inhomogeneities in the growth rate and saturation conditions across the ALD reactor. To probe and control for the effect of the direction of gas flow, the sample was rotated 180 ˚C in the chamber after the first 400 cycles.

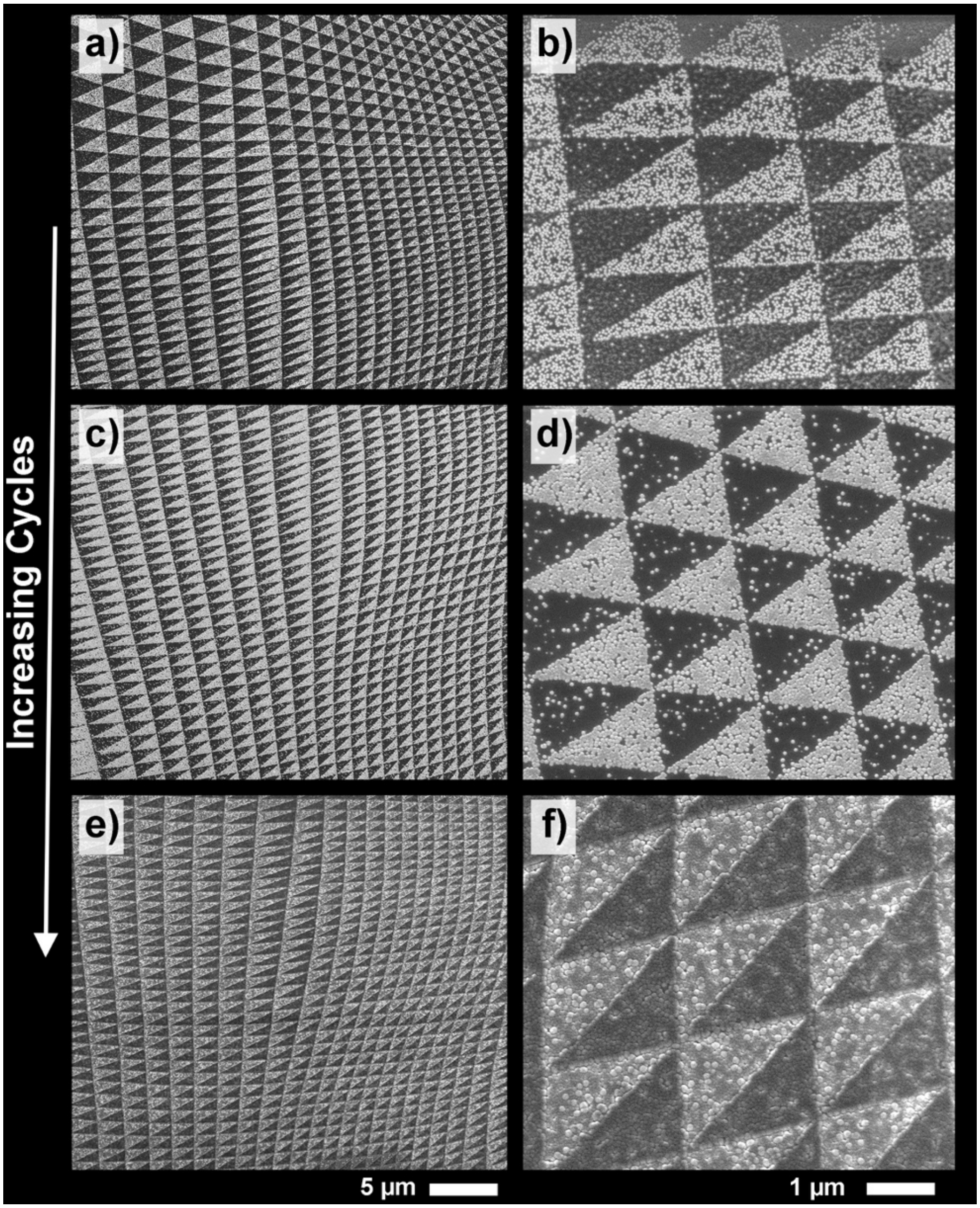

Figure 1-4. SEM images showing the evolution of a deposition pattern after (a,b) 200, (c,d) 400, and (e,f) 1000 cycles, respectively. After 400 cycles, the sample was rotated 180° in the ALD chamber to probe for gas directionality effects on the orientation of the deposition. Scale bar is 5 μm for the left column and 1 μm for the right column.

At a fixed ALD condition, inhomogeneities in the deposition rate are indicative of differences in reactivity among surface sites on the basal plane. The sequential deposition experiment indicates that some areas within the basal surface of mechanically exfoliated MoS_2 contain a network arrangement of two opposite-facing triangularly shaped regions that have mutually distinct deposition rates. Defects can introduce areas with modified densities of states and reactivities, so the emergence of the observed TiO_2 ALD pattern is consistent with the presence of an underlying defect network. These networks do not evolve over time and do not undergo deformation or transformation, showing that these disparate reactive regions are present prior to the ALD experiment and do not form *in situ*.

To determine if this phenomenon was unique to MoS_2 and TDMAT, we performed depositions onto HOPG and MoS_2 using both of $(EtCp)_2$ Mn as a MnO_x precursor and TDMAT. Figure 1-5 shows the presence of triangularly shaped deposition networks after ALD on mechanically exfoliated MoS_2 and HOPG with both precursors. All depositions were performed at 150 ˚C, but each recipe was optimized for the specific precursor and substrate. The recipes are as follows:

Figure 1-5a: 0.012 s(H_2O) – 15 s – 0.02 s(TDMAT) – 20 s (2)

Figure 1-5b: 0.01 s(H_2O) – 15 s – 0.02 s(TDMAT) – 20 s (3)

Figure 1-5c: 0.01 s(H_2O) – 30 s – 0.7 s($(EtCp)_2Mn$) – 30 s (4)

Figure 1-5d: 0.007 s(H_2O) – 30 s – 0.6 s($(EtCp)_2Mn$) – 30 s (5)

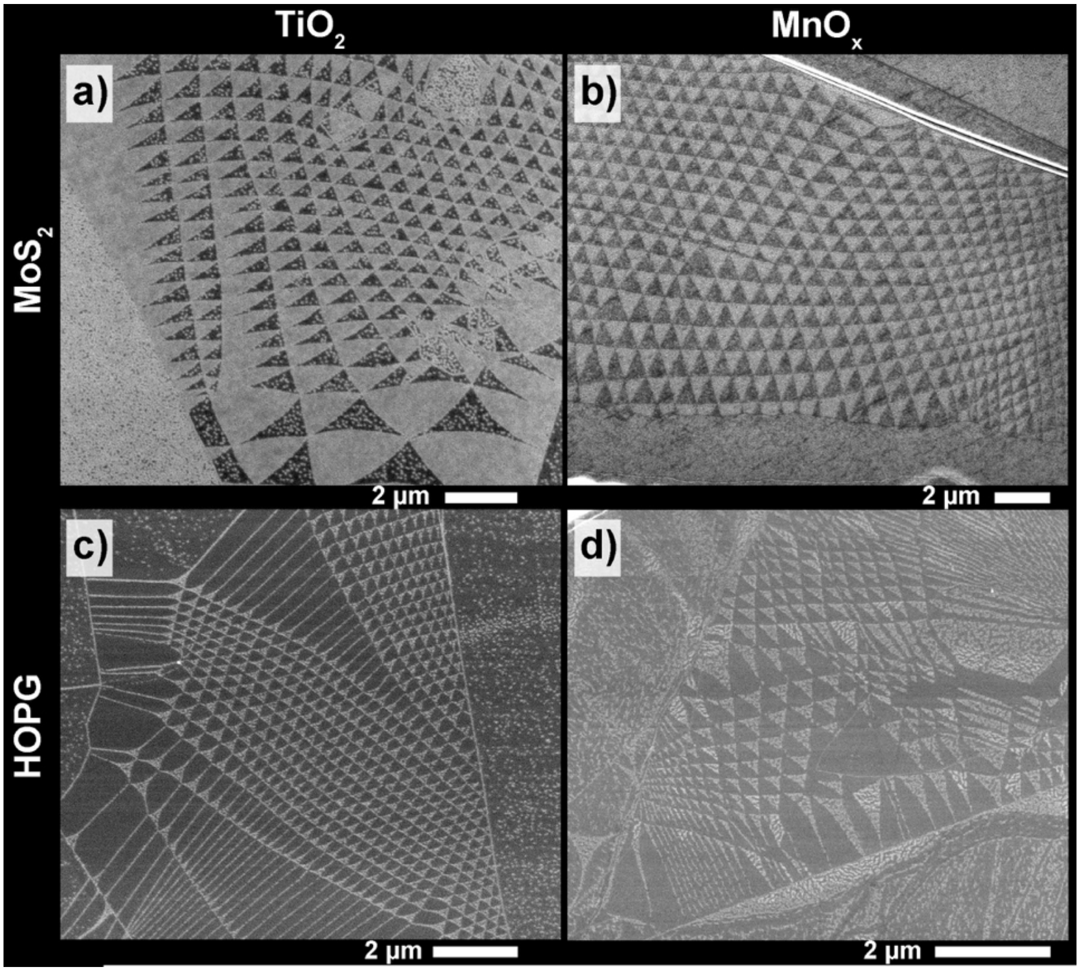

Figure 1-5. SEM images showing pattern development with different layered substrates and metal oxide precursors. A) The deposition of TiO_2 from TDMAT on MoS_2. B) MnO_x on MoS_2 from $(EtCp)_2Mn$. C) TiO_2 on HOPG. D) MnO_x on HOPG.

The ALD reaction conditions were tuned to access a low growth-rate regime, facilitating selective deposition of the network pattern. ALD with TDMAT on HOPG (Figure 1-5c) produced triangularly shaped deposition networks of a nominally identical morphology to those produced on MoS_2 (Figure 1-5a). The underlying mechanism enabling the formation of the patterns is thus independent of the specific bonding chemistry of the basal surface, suggesting that formation of the patterns is likely a general characteristic of 2D layered materials. Consistently, triangular networks with morphologies nominally identical to those produced on MoS_2 and HOPG using TDMAT were observed after ALD using $(EtCp)_2Mn$ on either MoS_2 or HOPG (Figure 1-5b,d). The observation of spontaneous network formation by manganese oxide (MnO_x) particles on the surface of mechanically exfoliated 2D materials strongly suggests that the mechanism of pattern formation is independent of the chemistry and structure of the metal organic precursor.

The inert nature of the pristine basal surface of 2D materials caused by the absence of dangling bonds hinders the deposition of films by ALD by preventing the facile adsorption of precursor molecules.[20,21] Bonding related defects, such as vacancies, act as high-energy sites facilitating precursor surface absorption and enhancing reactivity for deposition. However, bonding related defects within a single basal surface are random in nature and cannot explain the emergence of ordered deposits. In contrast, translational and rotational deformations to the van der Waals stacking of 2D layers induced by mechanical exfoliation can introduce local modifications to the stacking order that manifest as organized dislocation networks.[10] Dislocation networks caused by stacking order disruptions have been shown to modify the density of states, electrical conductivity, photoluminescence, and electronic structure of the layered material.[11,22-24] Thus, the presence of dislocation networks could introduce periodic regions with modified surface energy generating a reactivity landscape on the basal surface. The presence and morphology of dislocation networks on MoS_2 was therefore investigated to test the hypothesis that the triangularly shaped deposition network pattern on 2D layered materials resulted from the presence of defect networks in the exfoliated substrates.

While these highly-ordered network patterns were observed on naturally-occurring MoS_2 and polycrystalline HOPG purchased commercially, these network patterns were never observed on homemade, chemical vapor transport (CVT) synthesized MoS_2 or tungsten disulfide (WS_2). After 1000 ALD cycles at a low saturation condition t(TDMAT) = 0.025 s, single crystal CVT-synthesized flakes were imaged via optical microscopy. These samples are shown in Figure 1-6. In the case of the MoS_2 flake, the different colors indicate different thickness of TiO_2. Since deposition occurs more readily at edge sites, the TiO_2 film near the edges are a bright blue, relative to the basal plane shown in the yellow or purple regions. As a result, the flake is oriented as a series of ever-expanding triangular layers propagating downward. This structure is a clear indication of a screw-dislocation seeded growth mechanism.[25] In such a growth regime, MoS_2 layers are stacked directly on top of each other at each turn, resulting in a nearly perfect stacking registry generated during crystal growth. Such growth inhibits the defect-generation caused during mechanical exfoliation, and likely results in a separate exfoliation process where layers are "uncoiled" instead of ripped apart.[26] Such a process is also visible in the striking hexagonal pattern shown in the WS_2 crystal. This crystal was grown in a similar manner and displays the same screw-dislocation seeded behavior. The synthetic route and crystal structure makes the defect generation less likely in these structures. Future work may leverage more destructive exfoliation techniques, new synthetic routes, or a deliberate modification in the stacking arrangement to more reliably generate network patterns in synthetic materials.

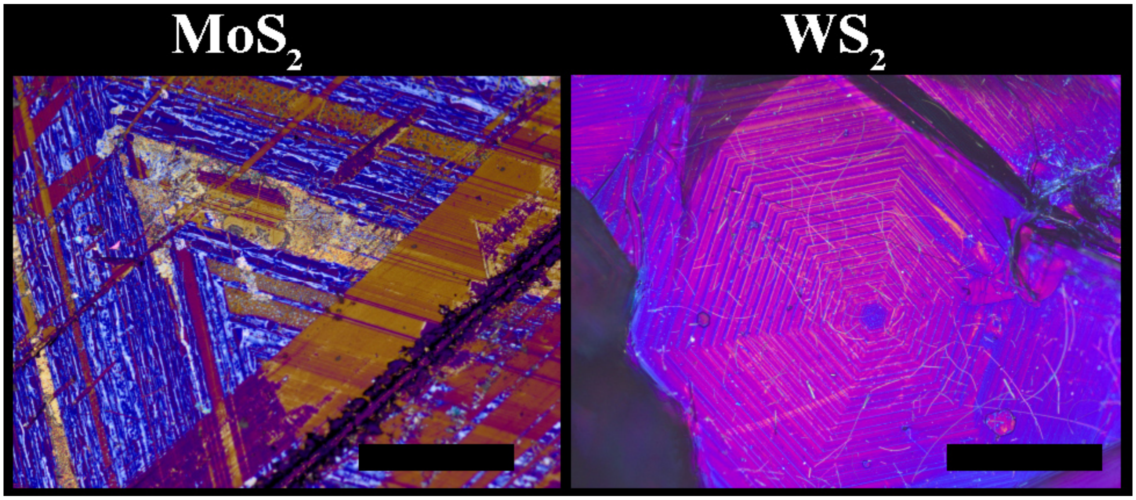

Figure 1-6. Real-color optical microscope images showing the screw-dislocation seeded growth of homemade CVT-synthesized samples. Regions in blue have the most deposited TiO_2 and regions in yellow have the least deposited TiO_2. Scale bars are 200 microns.

1.4 Transmission Electron Microscopy of Interrogated MoS_2 Flakes

Figure 1-7 shows TEM data obtained on an exfoliated MoS_2 flake transferred directly from tape to the TEM substrate. The high-resolution TEM data along the (001) zone axis shows the hexagonal lattice indicative of the 2H-phase MoS_2 most commonly found in naturally occurring molybdenite crystals (Figure 1-7a). The Fourier transform of the TEM image confirms this long-range ordered crystal structure (Figure 1-7b). Defects perpendicular to the basal plane and propagating through the van der Waals layers are observed as randomly dispersed point defects (Figure 1-7c). These defects do not form a dislocation network in the basal plane and are not responsible for the triangular or linear network deposits discussed in this text. A highly ordered dislocation network present over a large area is observed parallel to the basal plane and is arranged as a set of perfect dislocation lines (1-7d). This highly ordered dislocation network can introduce modifications to the stacking order of layers and result in defect-seeded growth across the basal plane.

Figure 1-8a shows an SEM image of a highly ordered line network pattern of TiO_2 deposits formed by ALD on MoS_2 via the recipe used in Figure 1-5a. The SEM pattern closely resembled the line pattern of dislocation networks observed by TEM on a mechanically exfoliated MoS_2 flake (Figure 1-8b and discussed above). The resemblance between the TiO_2 deposition pattern and the dislocation network pattern suggests that line defects generated by the disruptions in the stacking orientation of 2D layers during mechanical exfoliation can seed deposition under a range of low supersaturation conditions, and thus act similarly to the seeding effect of bonding-related defects. By analogy to previous studies on bonding-related defects,[27] 2D-stacking-related defects can therefore also serve as high-energy sites that lower the activation energy for heteronucleation, enabling preferential deposition under low supersaturation conditions.

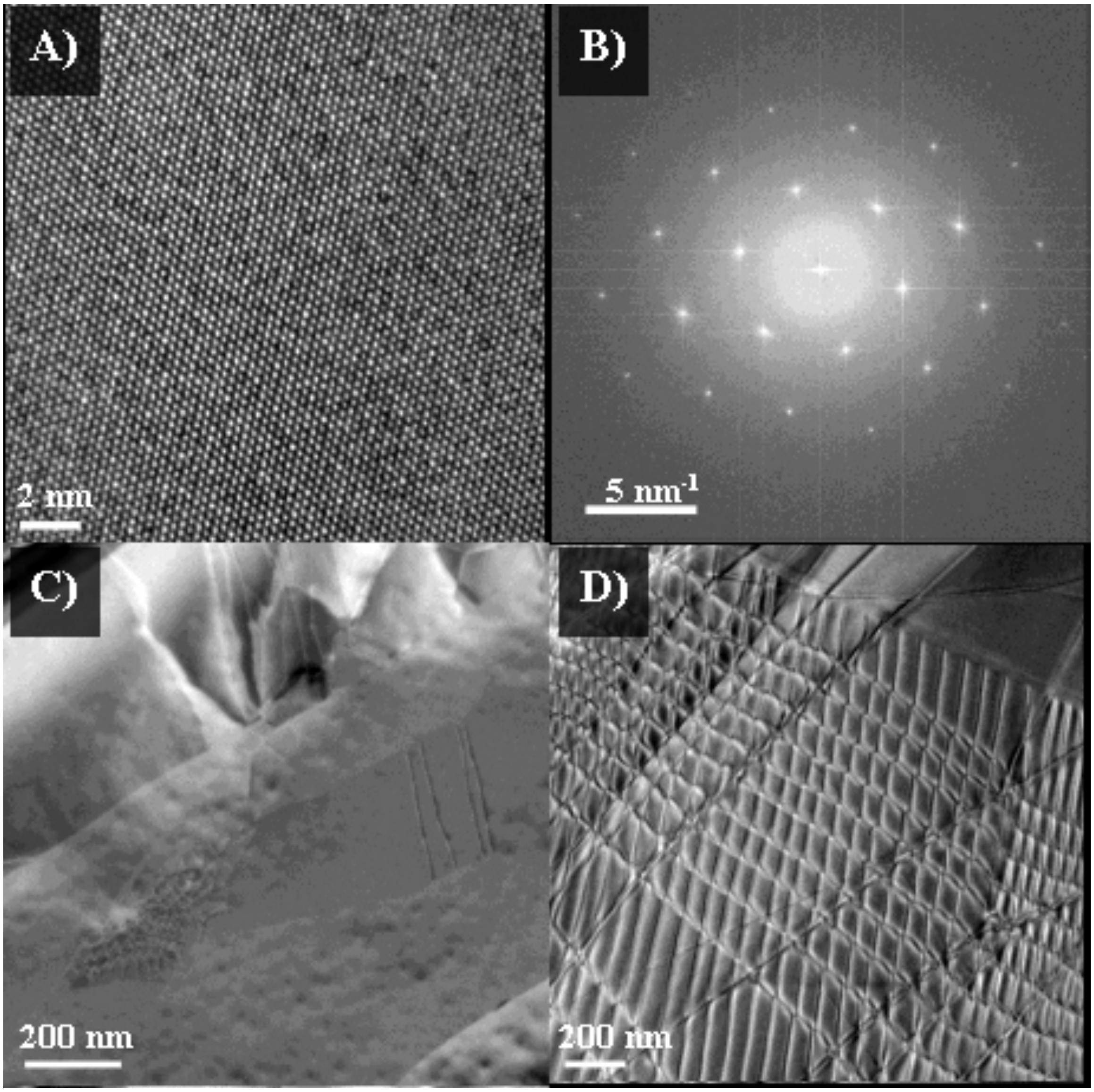

Figure 1-7. TEM analysis of an exfoliated MoS_2 flake. High-resolution TEM along the (001) Zone Axis (a). Fourier transform showing the long-range hexagonal crystal structure (b). Bright-field TEM perpendicular to the basal plane showing few defects (c). Bright-field TEM parallel to the basal plane showing a highly ordered dislocation network (d).

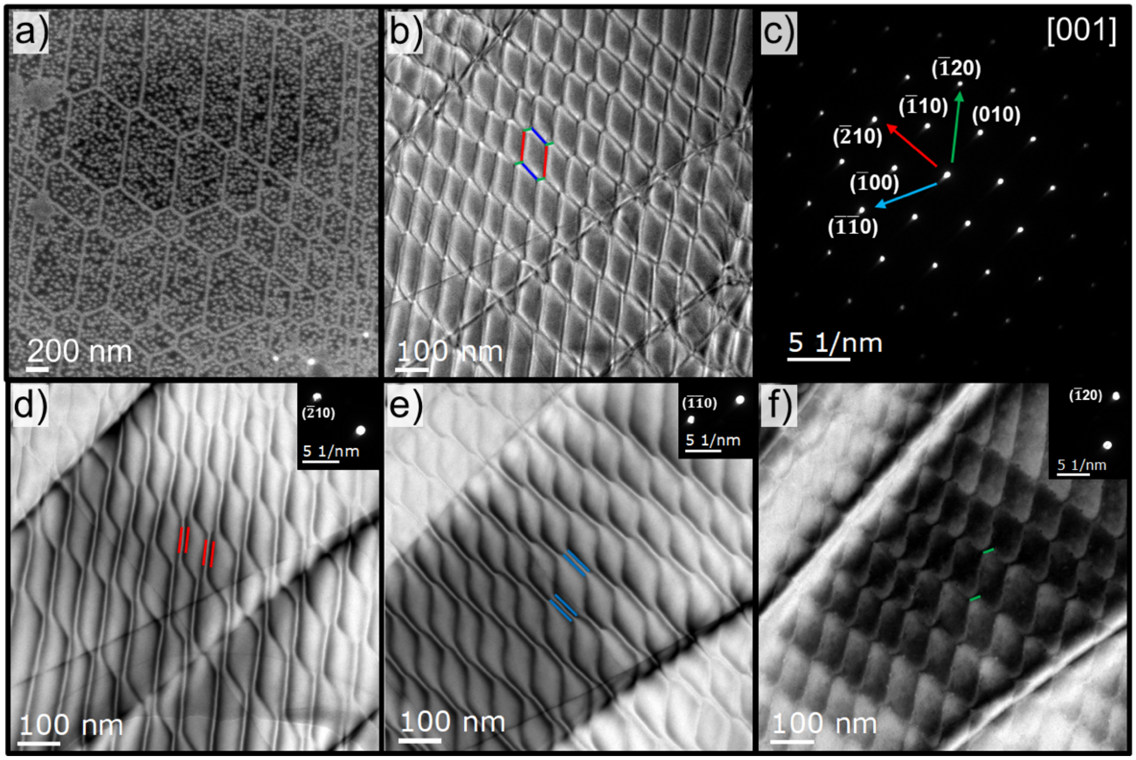

Figure 1-8. Relationship between patterned deposition and dislocation network. (a) SEM image of a TiO_2 deposition pattern in the shape of line networks on mechanically exfoliated MoS_2 observed after ALD. (b-c) TEM images and corresponding SAED pattern for a MoS_2 flake oriented along the [001] zone axis. Corresponding two-beam condition TEM images for the (d) $(\bar{2}10)$, (e) $(\bar{1}\bar{1}0)$, and (f) $(\bar{1}20)$ reciprocal lattice vectors.

The corresponding Burgers vectors (***b***) for the dislocation lines that spanned the network observed in Figure 1-8b were characterized by selecting perpendicular reciprocal lattice vectors (***g***) using a two-beam condition. In accordance with the invisibility criterion, the contrast of a dislocation vanishes when $\boldsymbol{g} \bullet \boldsymbol{b} = 0$, for dislocation contrast involving a single Bragg reflection. Figure 1-8d-f shows that selecting the ***g*** vectors $(\bar{2}10)$, $(\bar{1}\bar{1}0)$, and $(\bar{1}20)$ in a two-beam condition results in a contrast doubling for two (Figure 1-8d,e) out of three distinct undissociated dislocation lines, instead of the single vanishing contrast expected from the invisibility criterion. Contrast doubling under a two-beam condition is indicative of interactions between dislocations in the network (commonly known as interaction networks) and has been previously observed in naturally occurring MoS_2 (molybdenite).[28,29] In interaction networks, two Bragg reflections can be involved in the dislocation contrast, which causes a contrast doubling when selecting perpendicular ***g*** vectors. Due to the convolution of the two Bragg reflections, their Burgers vectors cannot be definitively isolated.

The three undissociated dislocations observed by TEM meet at a single node, spanning the network observed in Figure 1-8b. The line dislocation network can be visualized as ordered corrugations within layers. This corrugation induces a mismatch between layers that can be described as undissociated edge dislocations caused by a buckled region.[30] Dissociation of a perfect edge dislocation into partial dislocations results in the formation of a stacking fault region bounded by the two partials. Consequently, as illustrated in Figure 1-9, the relationship between line dislocation networks and triangular networks can be visualized through the dissociation of the three line dislocations, which results in the formation of networks containing triangular extended stacking-fault nodes bounded by partial dislocations (Figure 1-9), as well as alternating with opposite-facing triangular regions where the stacking is not modified.[22,31,32]

The crystal solid can reduce the total stacking fault energy by curving the partial dislocation lines towards the stacking fault region. Consequently, the curvature of the partial dislocation lines depends on the energy of the stacking fault. Figure 1-9c shows how the stacking fault energy affects the curvature (R) of the partial dislocation lines and the size of the stacking fault node.[33,34] For a stacking fault energy equal to zero, the partial dislocation lines have zero curvature resulting in a pattern composed of perfectly equilateral triangular nodes. For stacking fault energies greater than zero, the partial dislocation lines curve inwards and the area of the stacking fault node gets smaller until it eventually collapses into the perfect dislocation lines at sufficiently high stacking fault energies.

Figure 1-9d-g shows SEM images of deposition networks composed of lines, concave triangles connected by lines, corner-sharing concave triangles, and corner-sharing perfectly equilateral triangles on exfoliated MoS_2. Triangles with concave side walls were observed for both the triangular deposits and the opposite-facing triangular voids, indicating that in some cases the stacking fault node appears to be less reactive than the pristine surface. Several types of stacking faults involving two to three types of stacking alignments have been theoretically identified for molybdenite,[28] but the electronic structure for multilayer disruptions has not been studied extensively. In bilayer 2D stacks, extended triangularly shaped stacking fault networks have recently been shown to exhibit unique electronic structure and properties stemming from the modified density of states (DOS) induced by the altered stacking registry.[30,35] Further understanding the density of states for stacking faults on 2D materials would provide additional insight into the reactivity effects due to these DOS differences.

In general, the observed morphologies highlighted in Figure 1-9d-g provide a direct connection and morphological relationship between the observed line and triangular deposits and indicate that both types of deposition patterns originate from the same type of interacting dislocation defect network. Hence, the networked triangular deposition pattern observed after ALD on the basal surface of 2D materials can be explained as a result of preferential seeding induced by the presence of extended triangular stacking-fault nodes and pristine opposite-facing surfaces under low supersaturation conditions.

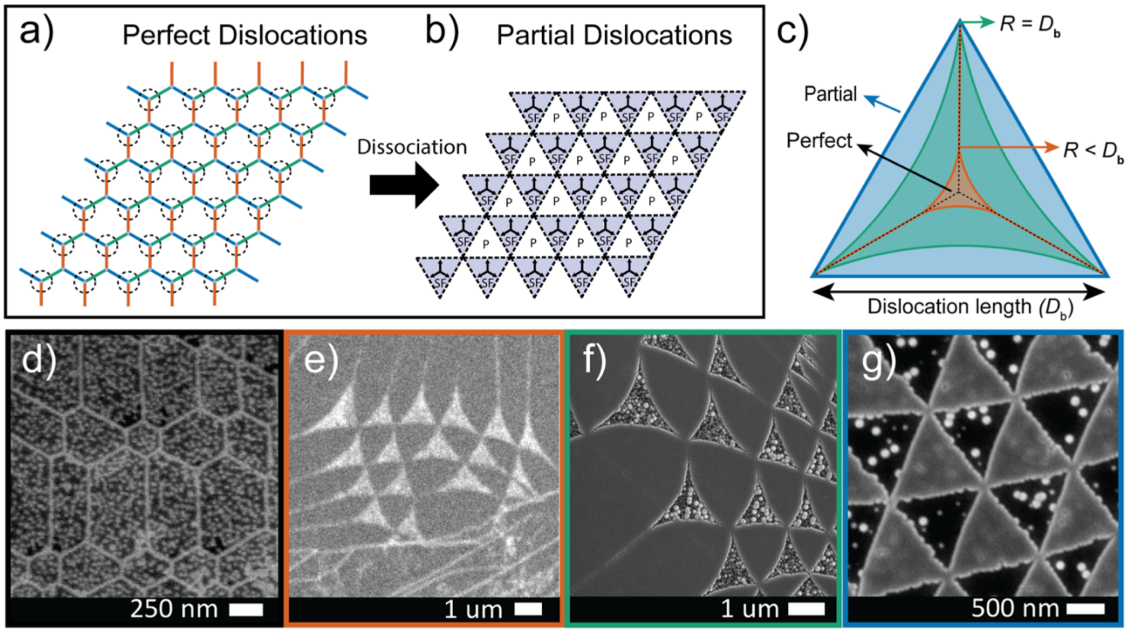

Figure 1-9. Relationship between stacking fault energy and patterned deposition. (a) Schematic of dislocation network highlighting the nodes that undergo extension after dissociation of the dislocations into partials. (b) Network of extended stacking-fault (SF) node regions (shaded triangles) composed of alternating SF triangles and opposite-facing triangles composed of pristine (P) surface (unshaded triangles). (c) Schematic showing that higher SF surface energies result in a decrease in the radius of curvature (*R*) of the dissociated partial dislocations and a decrease in the relative size of the triangular node. Note that in the schematics, the three distinct dislocations were assumed to be of equal length (D_b). SEM images of (d) line deposits, (e-f) triangular deposits and empty triangular voids with curved side walls, (f) and equilateral triangular deposits on exfoliated MoS_2.

1.5 Further Detail Concerning the Dislocation Network in Figure 1-8

In Figure 1-8, the individual color-coded dislocations are illustrated with two parallel lines. Disruptions to the Van der Waals stacking in 2D materials can result in the formation of dislocation networks. These distinct networks are given the labels **PQ, RP,** and **RQ.** As documented before in layered materials, interactions between dislocations can result in the formation of double contrast due to multiple Bragg reflections being satisfied. The schematic given in Figure 1-10 shows an interaction network with lines A and B formed by contrast involving two simultaneous Bragg reflections. In Figure 1-10b, the crossing points preserve the relative position of lines A and B and are labelled as nodes 1, 3, and 5 (N1, N3, and N5, respectively). Further interaction networks have been observed in naturally-occurring molybdenite crystals as described in Figure 1-10c. In this condition, there are no crossing points, resulting in a change of the relative positions of lines A and B and representing an apparent break in symmetry. It has been proposed that such segments are still present but are not visible due to the presence of extinction contours. An interaction network of this character is visible in Figure 1-8.

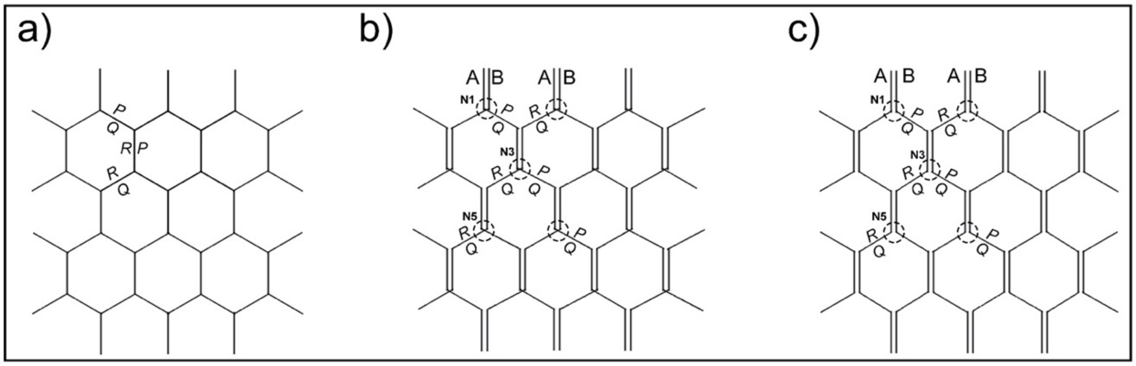

Figure 1-10. Diagram of observed interaction networks. (a) Dislocation network composed of three undissociated dislocations with Burgers vectors **PQ**, **RP**, and **RQ**. (b) Interaction network with crossing points. (c) Interaction networks without visible crossing points.

1.6 Atomic Force Micrographs Concerning Unusual Pattern Deposition in Figure 1-8f

Figure 1-8f describes a selective deposition condition wherein the concave-facing triangular voids are less reactive than the convex-facing regions. These concave-facing regions represent stacking faults with a stacking fault energy greater than zero, as described above. However, it is important to note that the stacking registry and atomic reconstruction within the stacking fault region is not known. Without detailed knowledge of the atomic arrangement of the stacking fault, the relative reactivity of different regions with respect to ALD precursors is not known. There exists within this network a stacking registry in the concave-facing regions that have a stacking fault energy greater than zero, but have a crystal structure that results in a more inert surface with respect to ALD precursors. This deposition behavior occurs frequently in this report, with concave-facing triangular voids found in Figure 1-5a. Additionally, AFM of this specific reaction condition is shown in Figure 1-11 and confirms the presence of these concave triangular voids.

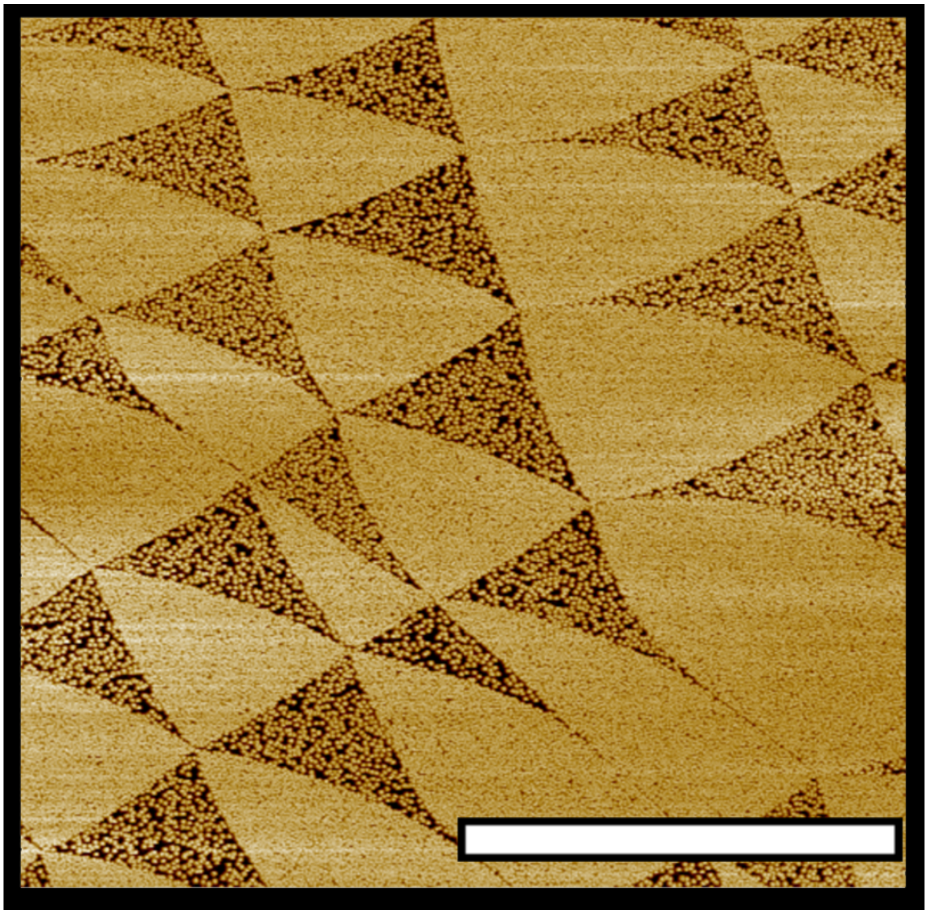

Figure 1-11. AFM data showing convex triangular deposits neighboring concave triangular voids. Nanoparticles are randomly distributed in the interior of the voids. Scale bar is 5 μm.

1.7 Conclusion and Future Outlook

Highly ordered triangular networks of metal-oxides spontaneously form on the surface of MoS_2 and HOPG during ALD. These networks form at a range of ALD supersaturation conditions and are independent of the number of ALD cycles. The presence of networks on both layered substrates and with MnO_x and TiO_2 precursors suggests that this deposition behavior is intrinsic to the 2D substrate. Dislocation networks are observed prior to ALD and line network deposits are observed after ALD. This is consistent with the hypothesis that basal plane defect networks introduce a surface reactivity landscape that can be exploited under a range of supersaturation conditions to produce patterned surfaces. This observed defect-seeded mechanism is likely general for 2D materials, and future work can expand on both the layered substrates studied as well as generating these patterns with other surface-sensitive deposition techniques such as electrodeposition.

1.8 References

1. Mak, K. F.; Lee, C.; Hone, J.; Shan, J.; Heinz, T. F. Atomically Thin MoS_2 : A New Direct-Gap Semiconductor. *Physical Review Letters* **2010,** *105* (13), 136805.

2. Velický, M.; Bissett, M. A.; Woods, C. R.; Toth, P. S.; Georgiou, T.; Kinloch, I. A.; Novoselov, K. S.; Dryfe, R. A. W. Photoelectrochemistry of Pristine Mono- and Few-Layer MoS_2. *Nano Letters* **2016,** *16* (3), 2023-2032.

3. Lee, J.-U.; Kim, K.; Han, S.; Ryu, G. H.; Lee, Z.; Cheong, H. Raman Signatures of Polytypism in Molybdenum Disulfide. *ACS Nano* **2016,** *10* (2), 1948-1953.

4. Ding, Q.; Song, B.; Xu, P.; Jin, S. Efficient Electrocatalytic and Photoelectrochemical Hydrogen Generation Using MoS_2 and Related Compounds. *Chem* **2016,** *1* (5), 699-726.

5. Jaramillo, T. F.; Jørgensen, K. P.; Bonde, J.; Nielsen, J. H.; Horch, S.; Chorkendorff, I. Identification of Active Edge Sites for Electrochemical H_2 Evolution from MoS_2 Nanocatalysts. *Science* **2007**, *317* (5834), 100–102.

6. Zhou, J.; Qin, J.; Guo, L.; Zhao, N.; Shi, C.; Liu, E.-z.; He, F.; Ma, L.; Li, J.; He, C. Scalable Synthesis of High-Quality Transition Metal Dichalcogenide Nanosheets and Their Application as Sodium-Ion Battery Anodes. *Journal of Materials Chemistry A* **2016,** *4* (44), 17370-17380.

7. Lin, D.; Liu, Y.; Liang, Z.; Lee, H.-W.; Sun, J.; Wang, H.; Yan, K.; Xie, J.; Cui, Y. Layered Reduced Graphene Oxide with Nanoscale Interlayer Gaps as a Stable Host for Lithium Metal Anodes. *Nature Nanotechnology* **2016**, *11* (7), 626–632.

8. Jariwala, D.; Davoyan, A. R.; Tagliabue, G.; Sherrott, M. C.; Wong, J.; Atwater, H. A. Near-Unity Absorption in van der Waals Semiconductors for Ultrathin Optoelectronics. *Nano Letters* **2016,** *16* (9), 5482-5487.

9. Yu, W. J.; Vu, Q. A.; Oh, H.; Nam, H. G.; Zhou, H.; Cha, S.; Kim, J.-Y.; Carvalho, A.; Jeong, M.; Choi, H.; Castro Neto, A.H.; Lee, Y.H.; Duan, X. Unusually Efficient Photocurrent Extraction in Monolayer van Der Waals Heterostructure by Tunnelling through Discretized Barriers. *Nature Communications* **2016**, *7* (1), 1–9.

10. Ly, T. H.; Zhao, J.; Keum, D. H.; Deng, Q.; Yu, Z.; Lee, Y. H. Hyperdislocations in van der Waals Layered Materials. *Nano Letters* **2016,** *16* (12), 7807-7813.

11. Bampoulis, P.; Sotthewes, K.; Siekman, M. H.; Zandvliet, H. J. W. Local Conduction in $MoxW_1–xSe_2$: The Role of Stacking Faults, Defects, and Alloying. *ACS Applied Materials & Interfaces* **2018,** *10* (15), 13218-13225.

12. Li, Z.; Yan, X.; Tang, Z.; Huo, Z.; Li, G.; Jiao, L.; Liu, L.-M.; Zhang, M.; Luo, J.; Zhu, J. Direct Observation of Multiple Rotational Stacking Faults Coexisting in Freestanding Bilayer MoS_2. *Scientific Reports* **2017,** *7* (1), 8323.

13. Cusati, T.; Fortunelli, A.; Fiori, G.; Iannaccone, G. Stacking and Interlayer Electron Transport in MoS_2. *Physical Review B* **2018,** *98* (11), 115403.

14. Johnson, R. W.; Hultqvist, A.; Bent, S. F. A Brief Review of Atomic Layer Deposition: From Fundamentals to Applications. *Materials Today* **2014,** *17* (5), 236-246.

15. Hu, S.; Shaner, M. R.; Beardslee, J. A.; Lichterman, M.; Brunschwig, B. S.; Lewis, N. S. Amorphous TiO_2 Coatings Stabilize Si, GaAs, and GaP Photoanodes for Efficient Water Oxidation. *Science* **2014,** *344* (6187), 1005.

16. Bobb-Semple, D.; Nardi, K. L.; Draeger, N.; Hausmann, D. M.; Bent, S. F. Area-Selective Atomic Layer Deposition Assisted by Self-Assembled Monolayers: A Comparison of Cu, Co, W, and Ru. *Chemistry of Materials* **2019,** *31* (5), 1635-1645.

17. Lee, H.-B.-R.; Baeck, S. H.; Jaramillo, T. F.; Bent, S. F. Growth of Pt Nanowires by Atomic Layer Deposition on Highly Ordered Pyrolytic Graphite. *Nano Letters* **2013,** *13* (2), 457-463.

18. Kim, K.; Lee, H.-B.-R.; Johnson, R. W.; Tanskanen, J. T.; Liu, N.; Kim, M.-G.; Pang, C.; Ahn, C.; Bent, S. F.; Bao, Z. Selective Metal Deposition at Graphene Line Defects by Atomic Layer Deposition. *Nature Communications* **2014,** *5* (1), 4781.

19. Abendroth, B.; Moebus, T.; Rentrop, S.; Strohmeyer, R.; Vinnichenko, M.; Weling, T.; Stöcker, H.; Meyer, D. C. Atomic Layer Deposition of TiO_2 from Tetrakis(Dimethylamino)Titanium and H_2O. *Thin Solid Films* **2013**, *545*, 176–182.

20. Walter, T. N.; Lee, S.; Zhang, X.; Chubarov, M.; Redwing, J. M.; Jackson, T. N.; Mohney, S. E. Atomic Layer Deposition of ZnO on MoS_2 and WSe_2. *Applied Surface Science* **2019**, *480*, 43–51.

21. McDonnell, S.; Brennan, B.; Azcatl, A.; Lu, N.; Dong, H.; Buie, C.; Kim, J.; Hinkle, C. L.; Kim, M. J.; Wallace, R. M. HfO_2 on MoS_2 by Atomic Layer Deposition: Adsorption Mechanisms and Thickness Scalability. *ACS Nano* **2013**, *7* (11), 10354–10361.

22. Hattendorf, S.; Georgi, A.; Liebmann, M.; Morgenstern, M. Networks of ABA and ABC Stacked Graphene on Mica Observed by Scanning Tunneling Microscopy. *Surface Science* **2013**, *610*, 53–58.

23. Shearer, M. J.; Samad, L.; Zhang, Y.; Zhao, Y.; Puretzky, A.; Eliceiri, K. W.; Wright, J. C.; Hamers, R. J.; Jin, S. Complex and Noncentrosymmetric Stacking of Layered Metal Dichalcogenide Materials Created by Screw Dislocations. *Journal of the American Chemical Society.* **2017**, *139* (9), 3496–3504.

24. Arovas, D. P.; Guinea, F. Stacking Faults, Bound States, and Quantum Hall Plateaus in Crystalline Graphite. *Physical Review B* **2008**, *78* (24), 245416.

25. Meng, F.; Morin, S. A.; Forticaux, A.; Jin, S. Screw Dislocation Driven Growth of Nanomaterials. *Accounts of Chemical Research* **2013**, *46* (7), 1616–1626.

26. Zhao, Y.; Zhang, C.; Kohler, D. D.; Scheeler, J. M.; Wright, J. C.; Voyles, P. M.; Jin, S. Supertwisted Spirals of Layered Materials Enabled by Growth on Non-Euclidean Surfaces. *Science* **2020**, *370* (6515), 442–445.

27. Xie, J.; Liao, L.; Gong, Y.; Li, Y.; Shi, F.; Pei, A.; Sun, J.; Zhang, R.; Kong, B.; Subbaraman, R.; Christensen, J.; Cui, Y. Stitching H-BN by Atomic Layer Deposition of LiF as a Stable Interface for Lithium Metal Anode. *Science Advances* **2017**, *3* (11), eaao2170.

28. Hörl, E. M. Dislocations in Molybdenite. *Journal of Applied Physics* **1965**, *36* (1), 253–261.

29. Kamiya, Y.; Ando, K.; Nonoyama, M.; Uyeda, R. Dislocation Networks and Moiré Patterns of Molybdenite. *Journal of the Phyical. Society of Japan* **1960**, *15* (11), 2025–2035.

30. Butz, B.; Dolle, C.; Niekiel, F.; Weber, K.; Waldmann, D.; Weber, H. B.; Meyer, B.; Spiecker, E. Dislocations in Bilayer Graphene. *Nature* **2014**, *505* (7484), 533–537.

31. Takahashi, N.; Shiojiri, M.; Enomoto, S. High Resolution Transmission Electron Microscope Observation of Stacking Faults of Molybdenum Disulphide in Relation to Lubrication. *Wear* **1991**, *146* (1), 107–123.

32. Delavignette, P.; Amelinckx, S. Dislocation Patterns in Graphite. *Journal of Nuclear Materials* **1962**, *5* (1), 17–66

33. Yadav, S. K.; Shao, S.; Wang, J.; Liu, X.-Y. Structural Modifications Due to Interface Chemistry at Metal-Nitride Interfaces. *Scientific Reports* **2015**, *5* (1), 17380.

34. Dai, S.; Xiang, Y.; Srolovitz, D. J. Structure and Energy of (111) Low-Angle Twist Boundaries in Al, Cu and Ni. *Acta Materialia* **2013**, *61* (4), 1327–1337.

35. Alden, J. S.; Tsen, A. W.; Huang, P. Y.; Hovden, R.; Brown, L.; Park, J.; Muller, D. A.; McEuen, P. L. Strain Solitons and Topological Defects in Bilayer Graphene. *Proceedings of the National Academy of Sciences USA* **2013**, *110* (28), 11256.

Chapter 2

Precision Transfer and Crystallographic Analysis of Patterned Molybdenum Disulfide Nanoflakes

2.1 Introduction

Few-layer and two-dimensional (2D) materials such as graphene, hexagonal boron-nitride (hBN), and transition metal dichalcogenides (TMD's) contain an array of unique chemical and physical properties currently under investigation. Graphene, an isolated layer of graphite, has extremely high tensile strength and electrical conductivity, and is actively investigated for use in next-generation electronics and commercial acoustics.[1-4] Among the TMD's, molybdenum disulfide (MoS_2) is a 1.8 eV direct bandgap semiconductor in its monolayer form, therefore making it a heavily researched ultrathin material in the field of photovoltaics.[5] Few-layer and 2D materials represent an emerging and extremely varied class of materials that show immense promise across the fields of chemical sensing, spintronics, and ultrathin electronics.[6-8]

Graphene can be reliably grown through a chemical vapor deposition (CVD) method, although the quality of the grown film has yet to match the quality of graphene mechanically exfoliated with scotch tape.[9] TMD's have only recently been successfully synthesized, but are extremely expensive and are of inferior quality relative to their mechanically exfoliated counterparts.[10] As a result, basic scientific research into the fundamental properties of few-layered materials requires synthesis via arduous mechanical exfoliation. Such a process has only become more challenging as the device architectures under investigation have become more complex.

Expanding to the few-layer regime, twisted bilayer graphene (TBG) has experienced an explosive growth in interest due to its remarkable superconducting properties and twist-angle dependent electronic structure.[11] In this and related fields, Moiré superlattices are intentionally fabricated with precise twist angles to generate heterostructures with modified electronic properties.[12] In this chapter, and in related fields, Moiré superlattices refer to a lattice mismatch between two vertically stacked layers. These layers generate a constantly changing bilayer structure over large lateral distances, often tens of nanometers.[13] Therefore, a new electronic structure and new properties emerge directly out of the disrupted stacking registry, as the placement of atoms in a Moiré superlattice is unique relative to the ground state crystal structure. Fabricating Moiré superlattices is a laborious and low-yield task. The current fabrication procedure requires that a monolayer be broken in half, with one end picked up with a stamp, rotated a precise angle, and gently placed back on the stationary half without slipping.[14]

To that end, a field of high-precision deterministic transfer of 2D or few-layer materials (referred to here as "nanoflakes"), as well as their metal contacts, has developed to more reliably generate van der Waals structures and devices. The most common transfer, viscoelastic stamping, relies on a viscoelastic stamp attached to a micromanipulator and high-objective microscope lens.[15] In this process, nanoflakes are mechanically exfoliated onto a viscoelastic material. The stamp is then placed upside down on a microscope slide and brought into contact with the target substrate. After alignment with the micromanipulator and the microscope, the stamp is contacted to the substrate. The stamp is then slowly removed from the surface at a low enough rate for the stamp to flow as a liquid. The stamp separates from the nanoflake, leaving it adhered to the substrate. From this method, a variety of transfer systems have been developed, commonly utilizing a polymer and a heated microscope stage to leverage the glass transition temperature to pick up and later detach a nanoflake from the surface.[16] Recent work with respect to transferring metal contacts involves a silane surface treatment to reduce the adhesion between the evaporated metal contact and the sacrificial substrate.[17] After deposition, the contact can be picked up by a stamp and transferred to the nanoflake. With this understanding of the high-precision transfer of nanoflakes, we designed a new transfer system for crystallographic analysis of patterned MoS_2 nanoflakes.

While mapping and observing topological defects and dislocation networks are considered in the previous chapter, elucidating the true stacking registry and atomic reconstruction remains a challenge. Atomic layer deposition (ALD) and conductive atomic force microscopy (c-AFM), can identify stacking faults and crystallographic defects with modified reactivity and electronic structure, but cannot provide atomic-scale understanding of the crystal structure.[18,19] As a result, the stacking faults identified in MoS_2 and HOPG in Chapter 1 cannot be intentionally generated or studied in further detail. Describing the atomic reconstruction of such stacking fault defects will provide a necessary link between the modified reactivity described here and the novel electronic and physical properties of Moiré superlattices on nanoflakes.

Recent work has described the atomic reconstruction of Moiré superlattices on bilayer graphene and TMD's.[20.21] Under specific twist angle conditions, Moiré superlattices undergo relaxation, wherein the superlattice "beat pattern" relaxes into networked regions with altered stacking orders directly next to regions of ground state atomic registries. Such a process is analogous to the process of dislocations dissociating into stacking faults in bulk crystals. As a result, direct crystallographic analysis of patterned stacking fault regions in MoS_2 and HOPG nanoflakes will provide information necessary to intentionally synthesize van der Waals structures with such stacking order modifications and understand the chemical reactivity and electronic structure of the perturbed region.

To this end, this chapter details the development of a new precision transfer system. This chapter will contain the reasoning behind the transfer system, the necessary criterion for our system, and the results obtained. Discussions about the surface reconstruction of layered material are included, and future work on mapping and identifying stacking order modifications is considered.

2.2 Materials and Methods

Naturally occurring molybdenum disulfide (MoS_2) was purchased from 2D Semiconductors as well as from SPI supplies. Prior to deposition, samples were exfoliated multiple times with scotch tape (3M Company) or blue tape (Nitto Denko) to expose a clean, flat surface. There was no observed difference in deposition from use of different types of tape for this exfoliation step.

After a fresh, flat surface was exposed, the crystal was exfoliated with blue tape. The crystal stuck to the blue tape was then exfoliated several times between two layers of tape to create thin flakes across an approximately 1 cm^2 region on the tape. The tape was then pressed into a 10 mm^2 SiO_2/Si chip (90 nm SiO_2 on P-doped Si, Graphene Supermarket). The tape was then slowly removed and the transferred nanoflakes were investigated under an optical microscope.

The nanoflake samples were placed into a Cambridge Nanotech S200 ALD system. Depositions were performed with 20 sccm N_2 carrier gas at 150 ˚C and at a base pressure of ~1 Torr. Titanium dioxide (TiO_2) was deposited using Tetrakis(dimethylamido)titanium (IV) (TDMAT, 99.999%, Sigma Aldrich) heated to 75 ˚C. The counter reactant was 18.2 MΩ resistivity (Millipore) water at room temperature.

The small lateral surface size of the exfoliated nanoflakes required a modified ALD recipe. The recipe was as follows:

$$0.012\text{s } (H_2O) – 15 \text{ s} – 0.03\text{s (TDMAT)} – 20 \text{ s.} \qquad (1)$$

This recipe modification allowed for growth of TiO_2 on the basal plane of these materials while minimizing growth on the bottom side of the flakes. After 200 cycles, the samples were removed from the ALD and analyzed with scanning electron and optical microscopy.

Scanning electron microscopy was performed using a FEI Nova NanoSe 450 at accelerating voltages between 3 and 5 keV with a 5 mm working distance.

Transmission electron microscopy (TEM) was performed using a FEI Tecnai Polara (F30) TEM at an accelerating voltage of 200 keV. The nanoflakes detailed in this chapter were transferred to C-Flat Holey Carbon 1.2/1.3 200 mesh copper grids from Electron Microscopy Sciences.

2.3 Development of the Transfer System

The high-precision transfer system must accomplish several tasks. First it must generate a high yield of nanoflakes. Direct, all-dry transfers to TEM grids do not transfer nanoflakes in high enough yield, and the nanoflakes are generally too small to support the defect networks observed *via* ALD. Deposited nanoparticles in the opposite-facing triangular voids are approximately 100 nm in diameter (Figure 2-1a). All-dry transfers, like the one used to prepare TEM samples in Chapter 1, generate very small flakes, and all observed dislocation networks are too small. The defect network shown in Chapter 1 is reproduced in Figure 2-1b to compare the size of the networks on all-dry transferred nanoflakes to more commonly observed pattern feature sizes. As an analogy, we can assume that the ALD patterning process is a microscope with a maximum resolution of approximately 100 nm, and anything smaller will not result in pattern formation for dissociated triangular networks.

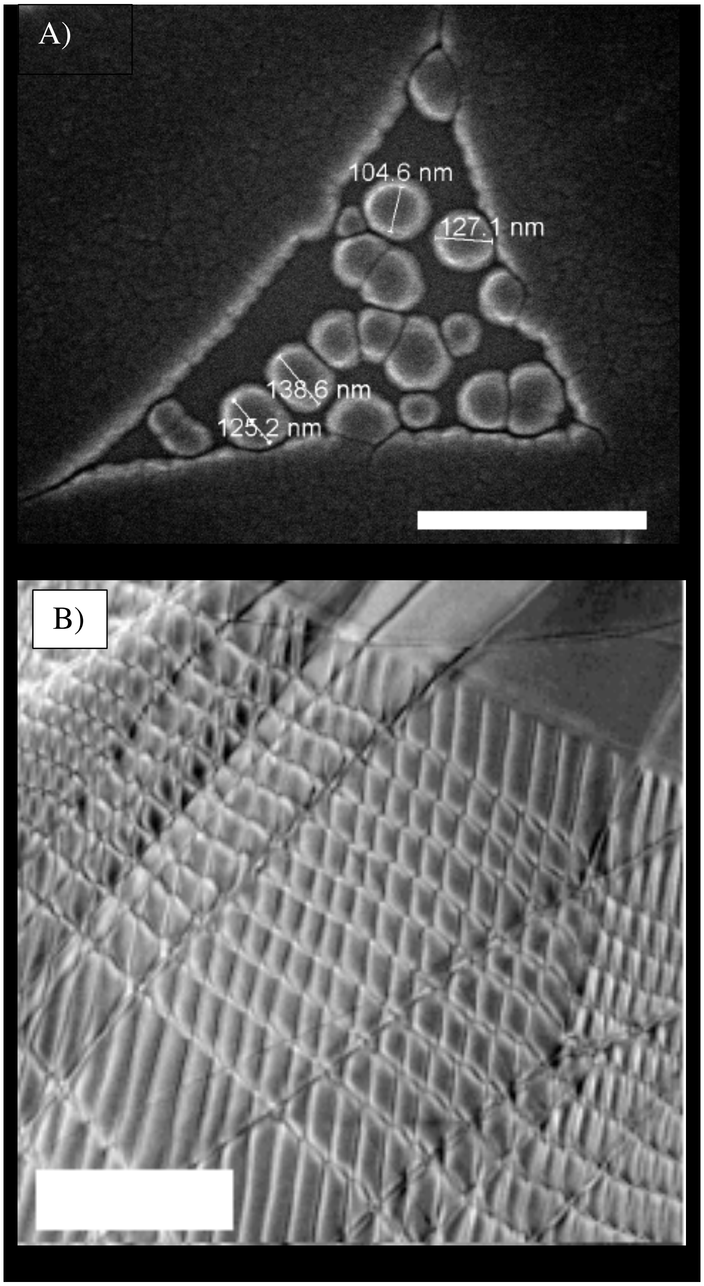

Figure 2-1. Limits of ALD patterning to detect dislocation networks. A) SEM image of an opposite-facing triangular void with size estimates of nanoparticle aggregates. B) Reproduced TEM image of a dislocation network. Scale bars are 500 nm.

The transfer system also cannot utilize a chemical etch step. Transfer of 2D-materials often utilizes an etch step to strip away a native oxide substrate for the exfoliated or transferred 2D-material.[22] ALD is used to observe the defect-driven reactivity, and the deposited metal oxides will instead be stripped away by such a step. Furthermore, any wet transfer step is unacceptable, since the triangular networked regions occupy a small fraction of the area of the nanoflake, hence there is no control over the orientation of the nanoflake on the holey-carbon TEM grid.

As a result, a transfer system was developed by combining techniques and equipment from different published transfer techniques to satisfy this specific condition. A cartoon of the transfer system is shown below in Figure 2-2.

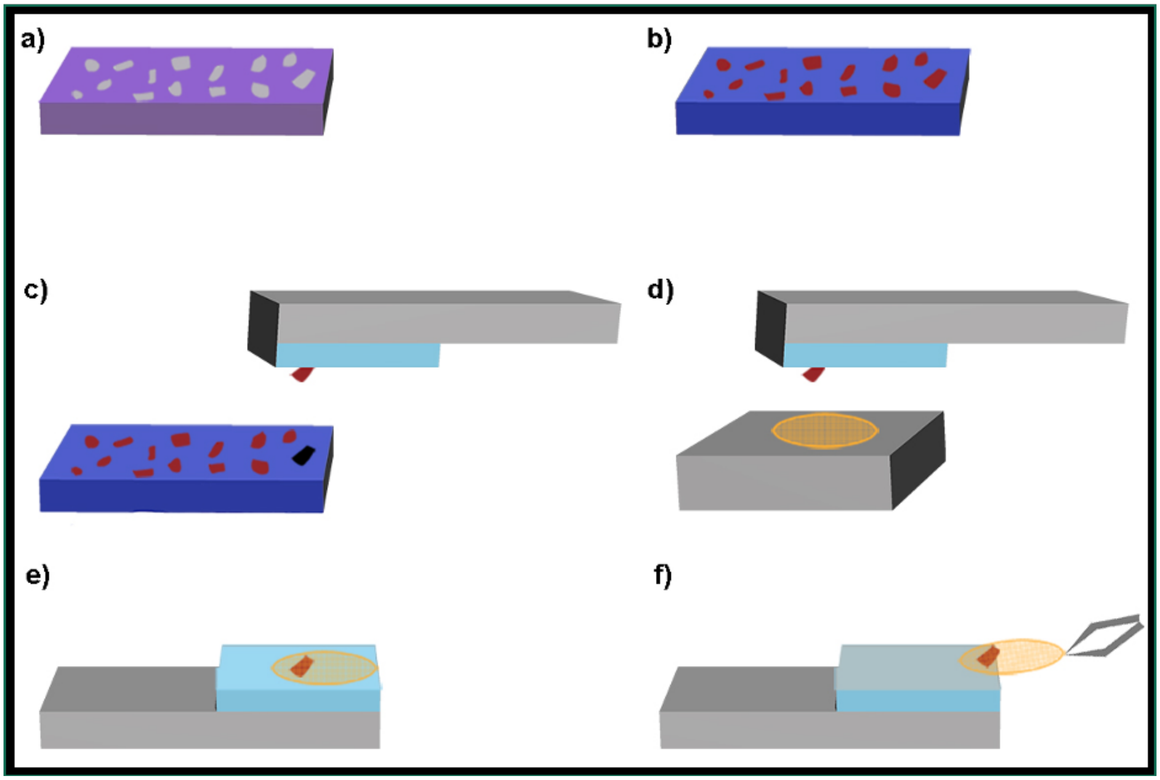

Figure 2-2. Schematic of the transfer system. A) Exfoliation of MoS_2 nanoflakes onto SiO_2 substrates. B) TiO_2 is deposited onto the nanoflakes *via* ALD. C) Patterned regions are found and picked up with a viscoelastic stamp. D) Flake is aligned over a TEM grid, and the stamp is pressed into the grid. E) The grid is strongly adhered to the gel through isopropanol evaporation. F) The grid is soaked in toluene and delaminates from the gel with the nanoflake.

The transfer system relies on exfoliation of MoS_2 nanoflakes directly onto SiO_2. This step increases the yield of thin, flat nanoflakes compared to the all-dry transfer sytem. The clean, flat SiO_2 surface allows more flakes to be exfoliated and adhered to the surface. Samples are then placed into the ALD reactor and exposed to 200 ALD cycles to deposit TiO_2. Nanoflakes are then investigated with SEM to locate samples with regions of patterned deposition. SEM images of patterned nanoflakes are shown in Figure 2-3.

Once nanoflakes of interest are identified, the flakes are then picked up by a viscoelastic stamp. While stamps are not commonly used to pick up flakes, multilayer nanoflakes can generally be picked up from SiO_2 substrates, as the van der Waals forces between the MoS_2 flake and the SiO_2 chip are relatively weak compared to the graphene/SiO_2 van der Waals interaction.[23] In this step, the viscoelastic stamp (Gel-Pak WF-X0/4/8) is adhered to a glass slide and pressed hard into the SiO_2 substrate and nanoflake of interest. Ideally, the nanoflake is near the center of the stamp. The stamp is then rapidly removed, carrying the nanoflake with it. This step relies on a weakly bound nanoflake on the surface, so corrugated nanoflakes will be more efficiently picked up than flat, well-adhered flakes. This step requires very rapid removal of the stamp. Once picked up, the flake and the stamp can be observed through an optical microscope. The stamp is then placed back on the viscoelastic stamping setup facing down. A TEM grid is placed beneath the stamp with the holey carbon support facing up. The stamp is slowly lowered onto the grid, while constantly adjusting the micromanipulators to keep the nanoflake in the center of the TEM grid. As the flake is lowered, the region with patterned deposition should not be near a copper support grid, but the other ends of the nanoflake must be over regions with the copper support. The stamp must be pressed into the TEM grid until a change in the optical contrast of the microscope shows that the holey carbon film is in contact with the stamp.

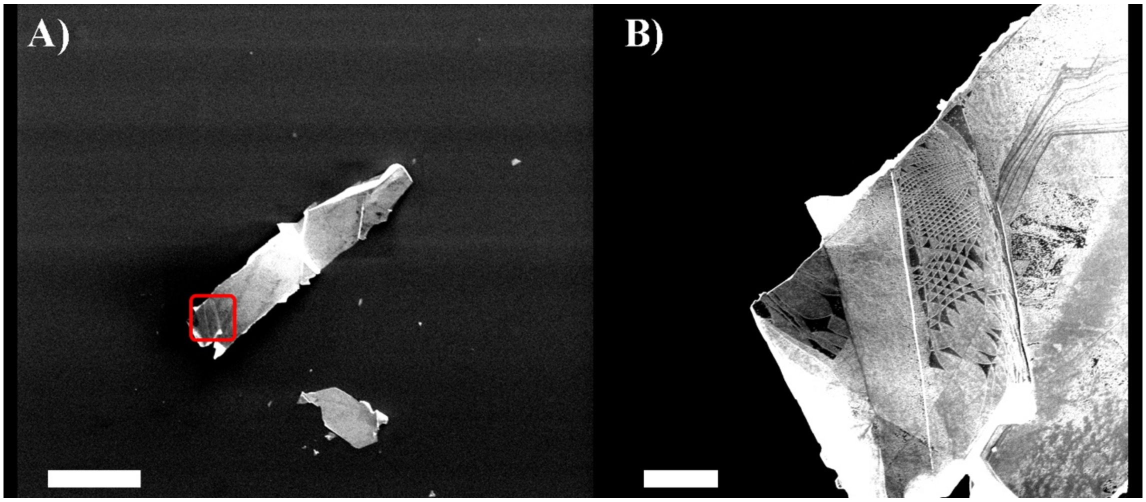

Figure 2-3. Observation of patterned deposition on nanoflakes. A) SEM image of a nanoflake on SiO_2 after 200 ALD cycles. B) SEM of the red inset region of the nanoflake with triangular deposition networks. Scale bars are 50 µm and 5 µm.

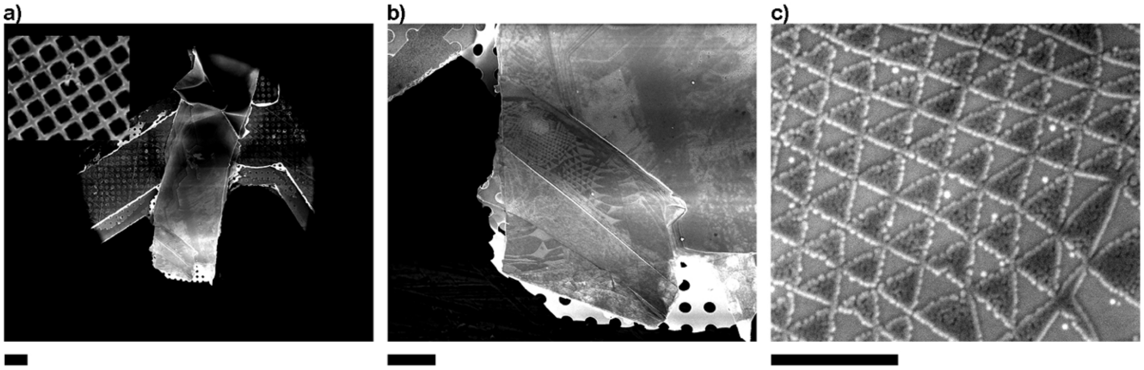

Figure 2-4. Observation of patterned deposition after transfer. A) SEM of the patterned nanoflake after successful transfer to the TEM grid. The inset shows the nanoflake deliberately placed in the center of the TEM grid. B-C) SEM images of the triangular network region after transfer. Scale bars are 10 µm, 5 µm, and 1 µm.

Previous reports have shown that TEM grids with holey carbon supports can be very strongly adhered to substrates through solvent evaporation.[24] The stamp is removed from the micromanipulator with the TEM grid weakly adhered. The stamp is flipped over to expose the TEM grid and a drop of isopropanol is placed on top of the grid and allowed to evaporate. As the droplet evaporates, surface tension strongly adheres the carbon foil to the viscoelastic stamp and nanoflake. The stamp is then moved to a hot plate set to 95 ˚C, and another isopropanol droplet is placed on top. The stamp is baked for half an hour to further promote adhesion.

Afterwards, optical inspection confirms that the TEM grid is strongly adhered to the stamp. The stamp is then placed face up in a petri dish containing approximately 15 mL of toluene. The petri dish is left partially covered overnight. Afterwards, the gelpak stamp has partially dissolved and the nanoflake is liberated from the surface along with the TEM grid. This process damages the holey carbon support and most of it is torn after transfer. Small amounts of gelpak and organic residue on the grid can be removed with a brief ozone treatment (approximately 10 mins) with the nanoflake facing up.

The power of this transfer system is shown in Figures 2-3 and 2-4. A region containing highly-ordered triangular network deposits was found on a large nanoflake exfoliated onto SiO_2. This nanoflake was picked up with a stamp and aligned directly on the circular ring at the center of a TEM grid. (Figure 2-4a and inset). The flake was free of any contaminants and the patterned region was off the side of the copper grid to allow for TEM analysis.

Optical micrographs detailing each step in this process can be found in Figure 2-5. This system allows for micron-scale control over the location and orientation of a transferred nanoflake. The small extended region on the southeast end of the flake in Figure 2-5a was the targeted transfer region. This flake was placed a few squares away from the center of the TEM grid and with the extended region facing off the copper support. The flakes sometimes transfer at a slight angle off the plane of the grid. This angle can be corrected for in the TEM instrument by tilting the grid during analysis.

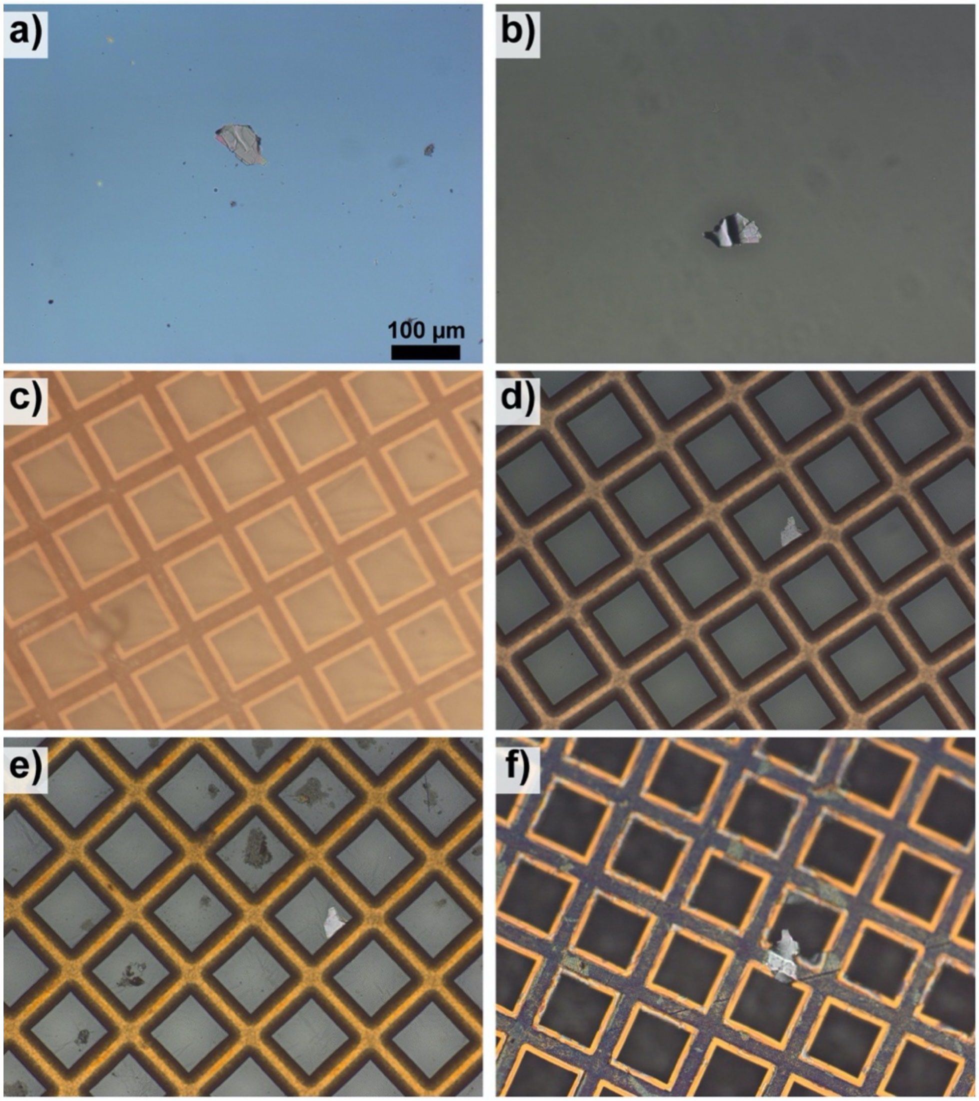

Figure 2-5. Images of a flake throughout the transfer processA) Optical images of a MoS_2 nanoflake in SiO_2 after ALD but prior to transfer. During this transfer, the small extended region on the southeast side of the flake was the simulated target area. B) The flake after being picked up by the stamp viewed from the opposite side from A). C) The nanoflake pressed into the TEM grid with the target area facing away from the copper support. D) Reverse side of the flake after the flake was weakly adhered to the TEM grid. E) Reverse side of the flake strongly adhered after the evaporative treatment. F) Successful transfer of the nanoflake with the target area off the copper grid after soaking overnight in toluene.

After transfer, additional TiO_2 deposition was performed to confirm that the transfer process did not alter the underlying crystal structure or the fundamental surface chemistry. Changes in the stacking order of layers or disruptions to the lattice would destroy the extended stacking fault network, removing the triangular deposition pattern. Additional organic residue would also provide nucleation sites on the already patterned surface, or covering the patterned network with contamination and result in a modified surface chemistry. Figure 2-6 shows a patterned nanoflake after transfer (Figure 2-6a) and after an additional 250 ALD cycles performed after transfer (Figure 2-6b). The pattern is clearly reinforced after depositon, confirming that the underlying crystal structure does not change throughout the process. If the crystal structure responsible for the patterned depositon were modified, the additional 250 ALD cycles would result in isotropic deposition, and the pattern would be replaced with more conformal film.

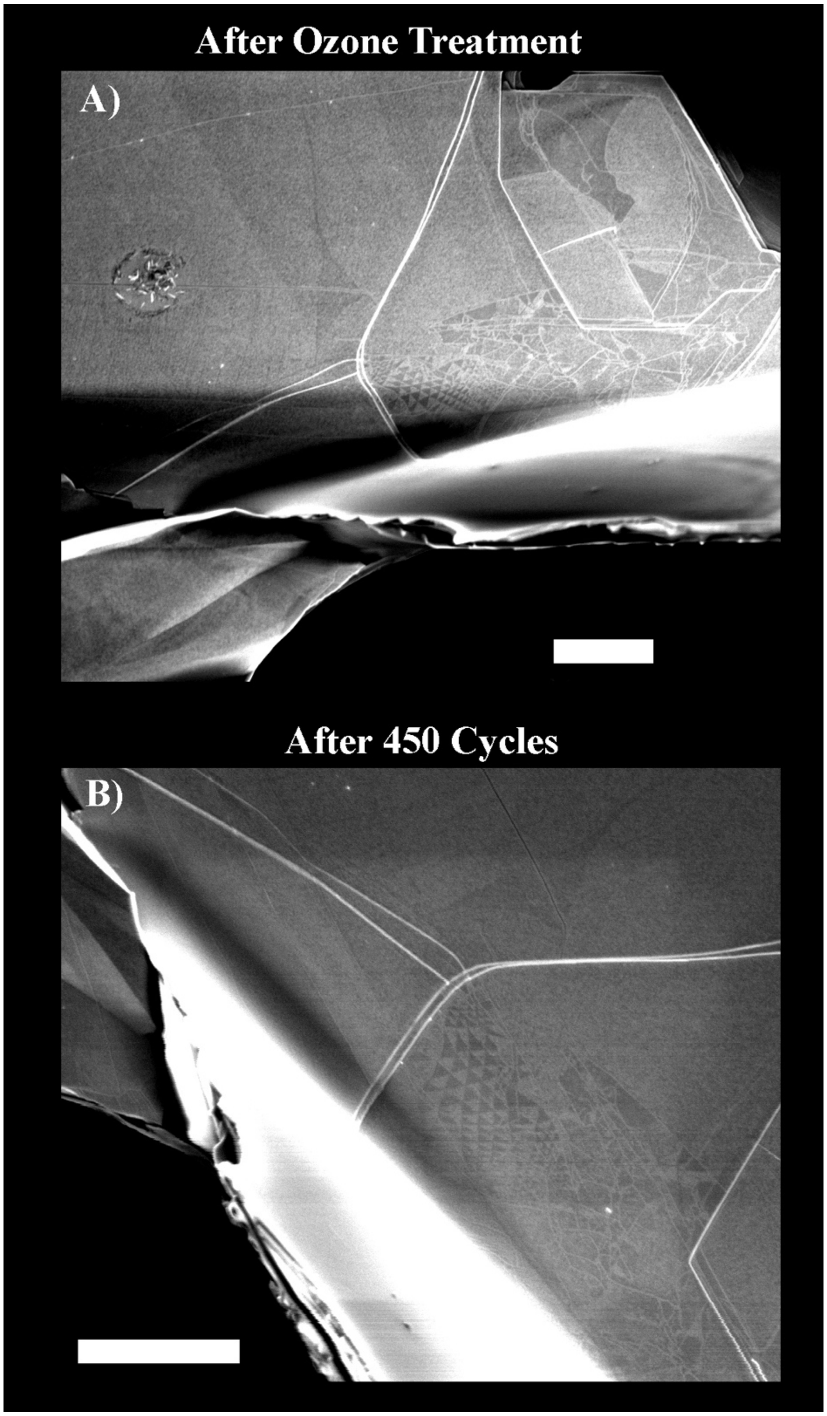

Figure 2-6. SEM image of a transferred nanoflake after ozone treatment (A). SEM image of the same nanoflake after 250 additional cycles after transfer showing that the pattern is preserved after transfer (B). Scale bars are 5 microns.

2.4 Transmission Electron Microscopy Analysis of Transferred Nanoflakes

TEM images of the deposition network shown in Figures 2-3 and 2-4 are shown in Figure 2-7. The amorphous TiO_2 films in the as-deposited triangular regions in Figure 2-7a more closely resemble nanoparticle aggregates than a conformal film. This packing behavior is expected for only 200 ALD cycles with a low TDMAT pulse time (see Figure 1-4a for comparison). The faint nanoparticles visible in the interiors are not present on the patterned surface, but rather on the film on the opposite end of the thin nanoflake. Figure 2-7b shows robust deposition on convex triangular regions with a well-defined boundary region on the edges of each triangle. On the edges of the triangular depositon network, the deposited TiO_2 resembles a close-packed film. This provides useful insight on the nature of the boundary layer between the deposited triangular networks and the inert concave regions. The edge of the stacking fault network in this figure is likely the most reactive region of the extended stacking fault network, given that the film is most dense in this region. Figures 2-7c and 2-7d show complex defect regions underneath the triangular deposition patterns, as evidenced by the ordered line networks. However, the depth of these networks and their role in seeding the growth of these patterns is not well known. During this experiment, we could not perform high-resolution TEM to monitor disruptions in the lattice. We could also not confirm the depth of the defect networks and map them onto the patterned region. This was primarily due to the extremely thin nanoflake imaged and the TiO_2 deposition on the reverse end which further limited TEM contrast.

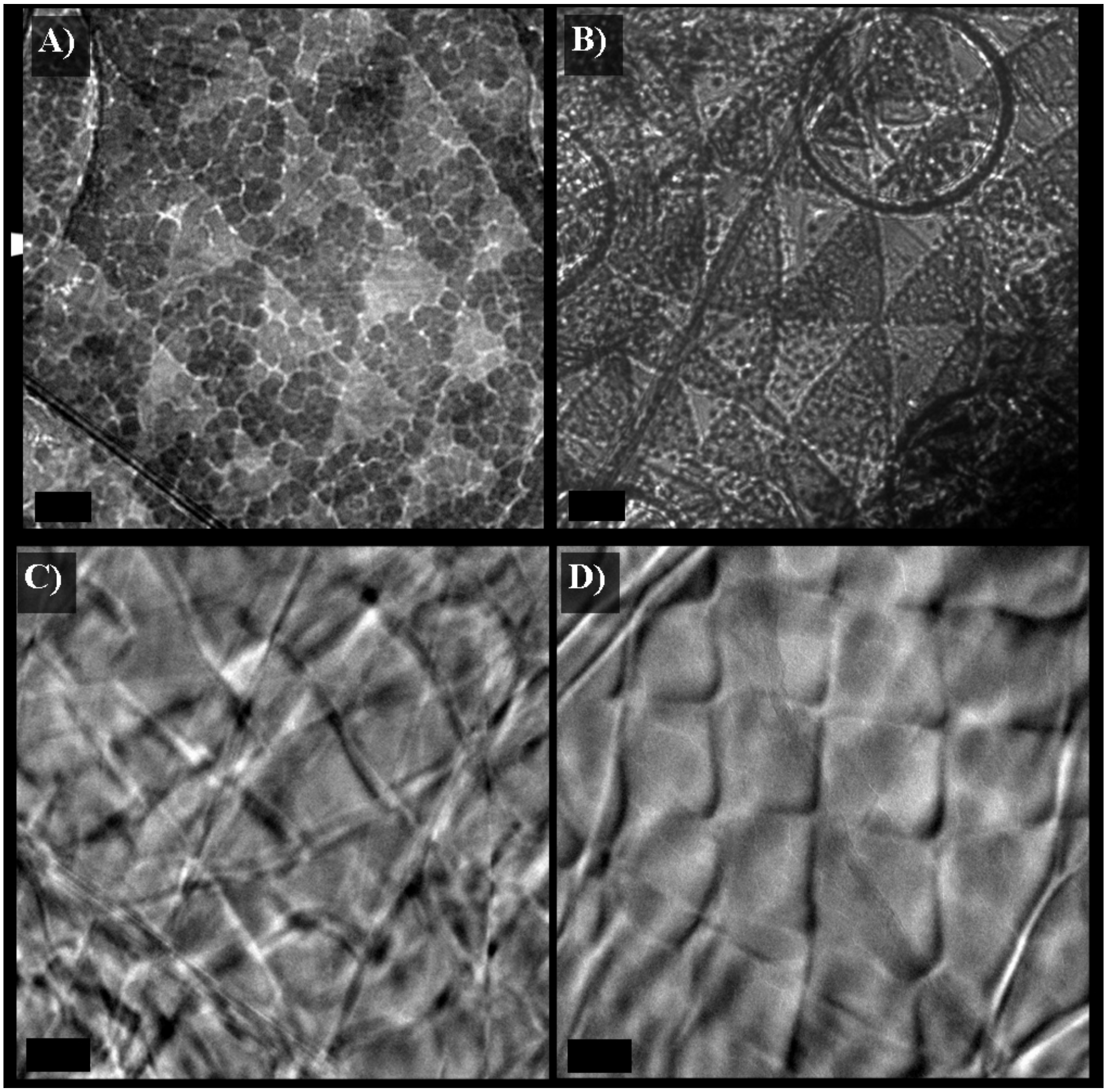

Figure 2-7. TEM analysis after transfer. A) TEM of the equilatteral triangular deposition network on a transferred MoS_2 nanoflake. B) TEM of a convex triangular deposition network on the same sample. C-D) TEM of defect network beneath the patterned regions. Scales bars are 100 nm, 200 nm, 100 nm, and 50 nm, respectively.

2.5 Conclusions and Future Outlook

A high-precision transfer system was developed to transfer patterned nanoflakes to TEM grids in a reliable, non-destructive manner. The developed system generates a high density of nanoflakes through mechanical exfoliation and allows for micron-scale precision orienting the nanoflake onto the TEM grid. TEM data provided important information about the nucleation chemistry of the ALD film as well as the film packing structure in the triangular deposited regions. Additional work will be required to improve reproducibility and probe the underlying crystal structure of the MoS_2 nanoflake. With some modifications to the technique, tuning the ALD recipe, and introducing post-processing cleaning steps, this approach can be implemented to directly probe the crystal structure responsible for the unusual patterned deposition described in this text.

2.6 Appendix I: Raman Mapping of Exfoliated Nanoflakes

Low-frequency Raman modes of MoS_2 and $MoSe_2$ nanoflakes have been shown to be sensitive to stacking order modifications.[25] While we lacked this capability on our instruments, we attempted to observe any raman peak shifting due to stacking order modifications across patterned MoS_2 nanoflakes. This was unsuccessful, but is worth noting here that the stacking faults responsible for defect-seeded ALD do not shift the A_{1g} and E_{2g} Raman modes in this experiment. Even with the very large triangular feature sizes and other large regions with little deposition (Figure S2-1a), there were no differences in the raman mode positions. There were no observable differences in the raman modes across the heterogenous flake.The flake may be too thick and the defect structure at the surface does not contribute to the overall raman spectrum enough to be observable. Regardless, it is important to note that spectroscopic techniques (Raman, photoluminescence, or X-Ray crystallography) may be able to determine changes in the underlying crystal structure without the difficult processing and transfer steps that TEM requires.

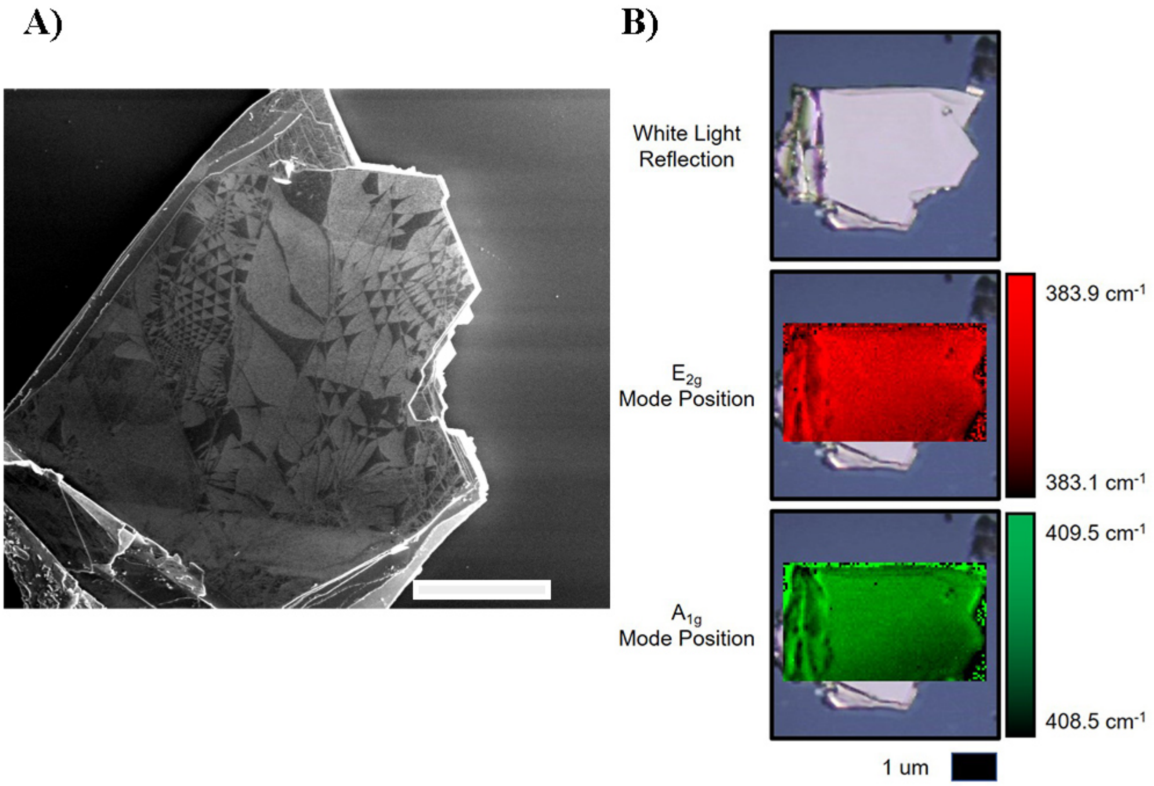

Figure S2-1. SEM image of an exfoliated nanoflake with large triangular network features. Scale bar is 10 microns. B) Raman map showing the position of the E_{2g} and A_{1g} raman modes across the MoS_2 nanoflake.

Appendix II: Outlook on the Transfer System

Given the incomplete nature of this project, it is easy to assume that this effort was fruitless. I will briefly argue for any intrepid readers that this work, while frankly extremely challenging, remains the most exciting project I worked on, and probably the most exciting time of my Ph.D research. Determining the atomic structure responsible for the triangular deposition networks is, without a doubt, the most exciting question posed by this work. It is also extremely difficult. Yield of triangular patterns on nanoflakes is very low, and this transfer system has an estimated 30-50 % success rate. By comparison to literature and anecdotal evidence, this rate is very good, but it still makes for a painful process. I am certain that a student/postdoc dedicated to iterating on this system, possibly introducing a new stamp such as a thermal release stamp, will yield better results. Using SiN TEM grids or performing a surface treatment on the SiO_2 to either increase yield or aid in the pick-up process would all be great avenues to explore. All told, we began working on transferring flakes around February 10, 2019, got the first successful transfer with this method around May 2019 and the first TEM images in June 2019. Several times while writing this chapter I was tempted to spend one or two more days in lab just trying to get this done. Any future student at Caltech or anywhere else interested in this problem is more than welcome to contact me, and I would love to consult and help whenever possible.

References

1. Mazilova, T. I.; Sadanov, E. V.; Mikhailovskij, I. M. Tensile Strength of Graphene Nanoribbons: An Experimental Approach. *Materials Letters* **2019**, *242*, 17–19.

2. Parvez, K.; Li, R.; Puniredd, S. R.; Hernandez, Y.; Hinkel, F.; Wang, S.; Feng, X.; Müllen, K. Electrochemically Exfoliated Graphene as Solution-Processable, Highly Conductive Electrodes for Organic Electronics. *ACS Nano* **2013**, *7* (4), 3598–3606.

3. Schwierz, F. Graphene Transistors. *Nature Nanotechnology* **2010**, *5* (7), 487–496.

4. Wei, Y.; Yu, G.; Li, X.; Shuai, H.; Ye, W.; Qiao, Y.; Tian, H.; Yang, Y.; Ren, T.-L. High Performance and Wireless Graphene Earphone towards Practical Applications. In *2020 4th IEEE Electron Devices Technology Manufacturing Conference (EDTM)*; 2020; pp 1–4.

5. Mak, K. F.; Lee, C.; Hone, J.; Shan, J.; Heinz, T. F. Atomically Thin MoS_2: A New Direct-Gap Semiconductor. *Physical Review Letters* **2010**, *105* (13), 136805.

6. Anichini, C.; Czepa, W.; Pakulski, D.; Aliprandi, A.; Ciesielski, A.; Samorì, P. Chemical Sensing with 2D Materials. *Chemical Society Reviews* **2018**, *47* (13), 4860–4908.

7. Roche, S.; Johan \AAkerman; Beschoten, B.; Charlier, J.-C.; Chshiev, M.; Dash, S. P.; Dlubak, B.; Fabian, J.; Fert, A.; Guimarães, M.; Guinea, F.; Grigorieva, I.; Schönenberger, C.; Seneor, P.; Stampfer, C.; Valenzuela, S. O.; Waintal, X.; Wees, B. van. Graphene Spintronics: The European Flagship Perspective. *2D Materials* **2015**, *2* (3), 030202.

8. Nourbakhsh, A.; Zubair, A.; Sajjad, R. N.; Tavakkoli K. G., A.; Chen, W.; Fang, S.; Ling, X.; Kong, J.; Dresselhaus, M. S.; Kaxiras, E.; Berggren, K. K.; Antoniadis, D.; Palacios, T. MoS2 Field-Effect Transistor with Sub-10 Nm Channel Length. *Nano Letters* **2016**, *16* (12), 7798–7806.

9. Drogowska-Horná, K.; Frank, O.; Kalbac, M. 10 - Chemical Vapor Deposition (CVD) Growth of Graphene Films. *Graphene (Second Edition)*; Skakalova, V., Kaiser, A. B., Eds.; Woodhead Publishing Series in Electronic and Optical Materials; Woodhead Publishing, 2021; pp 199–222.

10. Andrzejewski, D.; Marx, M.; Grundmann, A.; Pfingsten, O.; Kalisch, H.; Vescan, A.; Heuken, M.; Kümmell, T.; Bacher, G. Improved Luminescence Properties of MoS2 Monolayers Grown via MOCVD: Role of Pre-Treatment and Growth Parameters. *Nanotechnology* **2018**, *29* (29), 295704.

11. Cao, Y.; Fatemi, V.; Fang, S.; Watanabe, K.; Taniguchi, T.; Kaxiras, E.; Jarillo-Herrero, P. Unconventional Superconductivity in Magic-Angle Graphene Superlattices. *Nature* **2018**, *556* (7699), 43–50.

12. Yankowitz, M.; Jung, J.; Laksono, E.; Leconte, N.; Chittari, B. L.; Watanabe, K.; Taniguchi, T.; Adam, S.; Graf, D.; Dean, C. R. Dynamic Band-Structure Tuning of Graphene Moiré Superlattices with Pressure. *Nature* **2018**, *557* (7705), 404–408.

13. Abbas, G.; Li, Y.; Wang, H.; Zhang, W.-X.; Wang, C.; Zhang, H. Recent Advances in Twisted Structures of Flatland Materials and Crafting Moiré Superlattices. *Advanced Functional Materials* **2020**, *30* (36), 2000878.

14. Kim, K.; Yankowitz, M.; Fallahazad, B.; Kang, S.; Movva, H. C. P.; Huang, S.; Larentis, S.; Corbet, C. M.; Taniguchi, T.; Watanabe, K.; Banerjee, S. K.; LeRoy, B. J.; Tutuc, E. Van Der Waals Heterostructures with High Accuracy Rotational Alignment. *Nano Letters* **2016**, *16* (3), 1989–1995.

15. Castellanos-Gomez, A.; Buscema, M.; Molenaar, R.; Singh, V.; Janssen, L.; Zant, H. S. J. van der; Steele, G. A. Deterministic Transfer of Two-Dimensional Materials by All-Dry Viscoelastic Stamping. *2D Materials* **2014**, *1* (1), 011002.

16. Pizzocchero, F.; Gammelgaard, L.; Jessen, B. S.; Caridad, J. M.; Wang, L.; Hone, J.; Bøggild, P.; Booth, T. J. The Hot Pick-up Technique for Batch Assembly of van Der Waals Heterostructures. *Nature Communications* **2016**, *7* (1), 11894.

17. Went, C. M.; Wong, J.; Jahelka, P. R.; Kelzenberg, M.; Biswas, S.; Hunt, M. S.; Carbone, A.; Atwater, H. A. A New Metal Transfer Process for van Der Waals Contacts to Vertical Schottky-Junction Transition Metal Dichalcogenide Photovoltaics. *Science Advances* **2019**, *5* (12), eaax6061.

18. Mazza, M. F.; Cabán-Acevedo, M.; Wiensch, J. D.; Thompson, A. C.; Lewis, N. S. Defect-Seeded Atomic Layer Deposition of Metal Oxides on the Basal Plane of 2D Layered Materials. *Nano Letters* **2020**, *20* (4), 2632–2638.

19. Bampoulis, P.; Sotthewes, K.; Siekman, M. H.; Zandvliet, H. J. W. Local Conduction in $\mathrm{Mo}_{x}\mathrm{W}_{1-x}\mathrm{Se}_{2}$: The Role of Stacking Faults, Defects, and Alloying. *ACS Applied Materials & Interfaces* **2018**, *10* (15), 13218–13225.

20. Yoo, H.; Engelke, R.; Carr, S.; Fang, S.; Zhang, K.; Cazeaux, P.; Sung, S. H.; Hovden, R.; Tsen, A. W.; Taniguchi, T.; Watanabe, K.; Yi, G.-C.; Kim, M.; Luskin, M.; Tadmor, E. B.; Kaxiras, E.; Kim, P. Atomic and Electronic Reconstruction at the van Der Waals Interface in Twisted Bilayer Graphene. *Nature Materials* **2019**, *18* (5), 448–453.

21. Weston, A.; Zou, Y.; Enaldiev, V.; Summerfield, A.; Clark, N.; Zólyomi, V.; Graham, A.; Yelgel, C.; Magorrian, S.; Zhou, M.; Zultak, J.; Hopkinson, D.; Barinov, A.; Bointon, T. H.; Kretinin, A.; Wilson, N. R.; Beton, P. H.; Fal'ko, V. I.; Haigh, S. J.;

Gorbachev, R. Atomic Reconstruction in Twisted Bilayers of Transition Metal Dichalcogenides. *Nature Nanotechnology* **2020**.

22. Dauber, J.; Terrés, B.; Volk, C.; Trellenkamp, S.; Stampfer, C. Reducing Disorder in Graphene Nanoribbons by Chemical Edge Modification. *Applied Physics Letters* **2014**, *104* (8), 083105.

23. Magda, G. Z.; Pető, J.; Dobrik, G.; Hwang, C.; Biró, L. P.; Tapasztó, L. Exfoliation of Large-Area Transition Metal Chalcogenide Single Layers. *Scientific Reports* **2015**, *5* (1), 14714.

24. Regan, W.; Alem, N.; Alemán, B.; Geng, B.; Girit, Ç.; Maserati, L.; Wang, F.; Crommie, M.; Zettl, A. A Direct Transfer of Layer-Area Graphene. *Applied Physics Letters* **2010**, *96* (11), 113102.

25. O'Brien, M.; McEvoy, N.; Hanlon, D.; Hallam, T.; Coleman, J. N.; Duesberg, G. S. Mapping of Low-Frequency Raman Modes in CVD-Grown Transition Metal Dichalcogenides: Layer Number, Stacking Orientation and Resonant Effects. *Scientific Reports* **2016**, *6* (1), 19476.

Chapter 3

Selective-area, Water-Free Atomic Layer Deposition of Metal Oxides on Graphene Defects

Adapted From:

Mazza, M.F.; Cában-Acevedo M.C.; Fu, H.J.; Meier, M.C.; Thompson, A.C.; Ifkovits, Z.P., Carim, A.I.; Lewis, N.S. Selective-area, Water-Free Atomic Layer Deposition of Metal Oxides on Graphene Defects. ***ACS Materials Au*. 2021.**

3.1 Introduction

Since the isolation of mechanically exfoliated monolayer graphene in 2004, interest in graphene and other two-dimensional (2D) materials has grown rapidly.[1] Graphene, an atomically flat surface of sp^2-hybridized carbon atoms, is characterized by its extremely high tensile strength and high electrical conductivity.[2,3] Graphene can be synthesized *via* mechanical exfoliation, epitaxial growth on silicon carbide (SiC), and through chemical vapor deposition (CVD) on copper.[4-6] CVD-synthesized graphene remains the only large-scale, commercially feasible method out of these three techniques. CVD-synthesized graphene can be successfully fabricated at scale, but the quality of the graphene synthesized pales in comparison to the quality of graphene made through mechanical exfoliation of graphite. Further, CVD-synthesized graphene contains grain boundaries and defects that dramatically reduce the strength and electronic conductivity of the graphene sheet.[7,8] Moreover, graphene must be transferred from the copper substrate, and this transfer process introduces folds, wrinkles, and tears in the graphene sheet that further impede device performance.[9]

Atomic-layer deposition (ALD) is a low-cost and scalable method for deposition of metals, metal nitrides, and metal oxides.[10-12] ALD exploits self-limiting chemical reactions on the surface of the substrate, and results in highly conformal thin films with precise control of the resulting film thickness. Typically, ALD of metal oxides has been performed by introducing a metal-organic precursor molecule along with a counter reactant, often water or ozone, to decompose the precursor and produce a surface-terminated thin film. Conversely, selective-area ALD (sa-ALD) has been used to generate anisotropic and patterned depositions for device integration and catalytic layers.[13-14] Sa-ALD has been achieved by using self-assembled monolayers and chemical functional groups to block the ALD precursors from adsorbing onto specific regions of the substrate.[15] Patterned deposition has also been obtained using heterogeneous substrates or catalytic surface reactions.[16,17] Platinum metal has been selectively deposited onto line defects of graphene.[18] In contrast, deposition of metal oxides typically requires lower temperatures and supersaturation of the surface with a strong oxidant, such as water or ozone, leading to a reduction in selectivity.

This chapter discusses the development and investigation of sa-ALD onto CVD-graphene, highly-oriented pyrolytic graphite (HOPG), and exfoliated few-layer graphene. We report sa-ALD of both titanium oxide (TiO_2) and a mixed-metal oxide, aluminum titanium oxide ($Al_xTi_yO_z$) onto line defects and step edges of HOPG and graphene through a water-free recipe. The best results were achieved with the mixed-metal oxide and will be the primary focus of this chapter. The metal-oxygen bond was introduced *via* the titanium precursor (titanium(IV) iso-propoxide, TTIP), and a second metal-organic precursor was used as a counter-reactant to facilitate decomposition. This process prevents supersaturation of the graphene or graphite basal plane with a strong oxidant and relies instead on intrinsic reactivity differences between the defective regions of the graphene sheet and the inert basal plane.

3.2 Materials and Methods

CVD-grown graphene on Si was purchased from Advanced Chemicals Supplier Material (ACS Material) and was used as received. The Si substrate was doped p-type with a resistivity < 0.01 Ω cm. Monolayer graphene was grown on a Cu foil and transferred with a PMMA (poly methylmethacrylate) protection layer *via* a wet transfer process. The grain size of the as-deposited monolayer CVD-graphene film was ~ 50 μm prior to transfer.

Titanium dioxide (TiO_2) and aluminum oxide (Al_2O_3) were deposited using a Cambridge Nanotech S200 ALD system. All depositions were performed with 20 sccm N_2 carrier gas at a base pressure of ~ 0.6 torr. Titanium (IV) iso-propoxide (TTIP, 98% STREM) was heated to 75 ˚C and used as the titanium source. Trimethyl aluminum (TMA, 98% STREM) at room temperature was used as the aluminum source. For the pure TiO_2 film, Tetrakis(dimethylamido)titanium (IV) (TDMAT, 99.999% Sigma Aldrich), heated to 75 ˚C was used as the counter reactant instead of TMA. This pure titanium precursor combination deposited films with less selectivity and reproducibility, but are nonetheless discussed here.

HOPG was exfoliated with scotch tape (3M company) a few times to generate nanoflakes. The flakes were then transferred onto gold wafers by pressing the tape into the wafer and rapidly removing the tape. The thickness of each exfoliated few-layer sample was examined *via* optical microscopy.

The ALD recipe for the mixed-metal oxide deposition onto CVD-graphene was:

TTIP(0.013s) – 40s – TMA(0.011s) – 40s. (1)

The ALD control recipes for each water-based reaction are as follows:

TMA(0.011s) – 40s – H_2O (0.015s) – 40s. (2)

TTIP(0.013s) – 40s – H_2O(0.015s) – 40s. (3)

While the recipe for the pure titanium film was:

TTIP(0.013s) – 40s – TDMAT(0.025s)-40s. (4)

The deposition temperature for the pure titanium was 150 ˚C while the mixed-metal oxide deposition was performed at various temperatures and are noted in the text.

Scanning-electron microscopy (SEM) was performed using a FEI Nova NanoSE 450 at accelerating voltages between 3 and 15 keV with a 5 mm working distance.

X-ray photoelectron spectroscopy (XPS) was performed using a Surface Science M-probe ESCA/XPS. The system had a chamber base pressure of $<2 \times 10^{-8}$. The sample was illuminated by a 1486.7 eV Al Kα monochromatic x-ray source at 35˚ relative to the surface. Photoelectrons were collected by a hemispherical energy analyzer with a 100mm radius and a pass energy of 25 eV. The analyzer had a resolution of ~ 0.8 eV. Data were acquired using the ESCA25 Capture (Service Physics, Bend, OR; V5.01.04) software and were evaluated using CasaXPS software. The high-resolution peaks were referenced to the graphene carbon 1s peak at 284 eV.

Atomic-force microscopy (AFM) was performed using a Bruker Dimension Icon. Samples were affixed to a steel disc using Ag paint. The scan was performed with the PeakForce setpoint at 5.0 nN scan rate at 0.501 Hz, and a PeakForce amplitude at 150 nm using a SCM-PtSi (Bruker) probe with a nominal tip radius of 15 nm. PeakForce Kelvin

Probe Force Microscopy (PF-KPFM) was performed during the scan, in which height, adhesion, and potential maps were collected concurrently. Adhesion maps provided qualitative data comparing relative adhesion of the heterogeneous surface scanned and were not calibrated to a reference sample.

3.3 Selective Deposition onto HOPG and Few-Layer Graphene

HOPG, the bulk, three-dimensional (3D) form of graphene, is an excellent test material for a selective deposition technique. HOPG is cheap and easily processible and contains step edges and surface line defects that serve as high energy sites that seed nucleation.[19] The first recipe developed for water-free sa-ALD utilized a TTIP/TDMAT recipe to deposit pure TiO_2, and the preliminary results of this experiment are shown in Figure 3-1. Here, we report the highly ordered triangular patterns described in Chapter 1 (Figure 3-1a). Extended stacking fault networks serve as high-energy defect sites that can preferentially seed nucleation. Therefore, a defect selective ALD recipe should similarly result in pattern development due to the differences in reactivity between the stacking fault and the pristine surface. Figure 3-1b shows an SEM of the HOPG surface containing line defects or step edges that have been preferentially coated with TiO_2 along with small nanoparticles accumulating on the basal plane. This experiment works as a proof-of-concept, and the deposition was then expanded to mechanically exfoliated few-layer graphene.

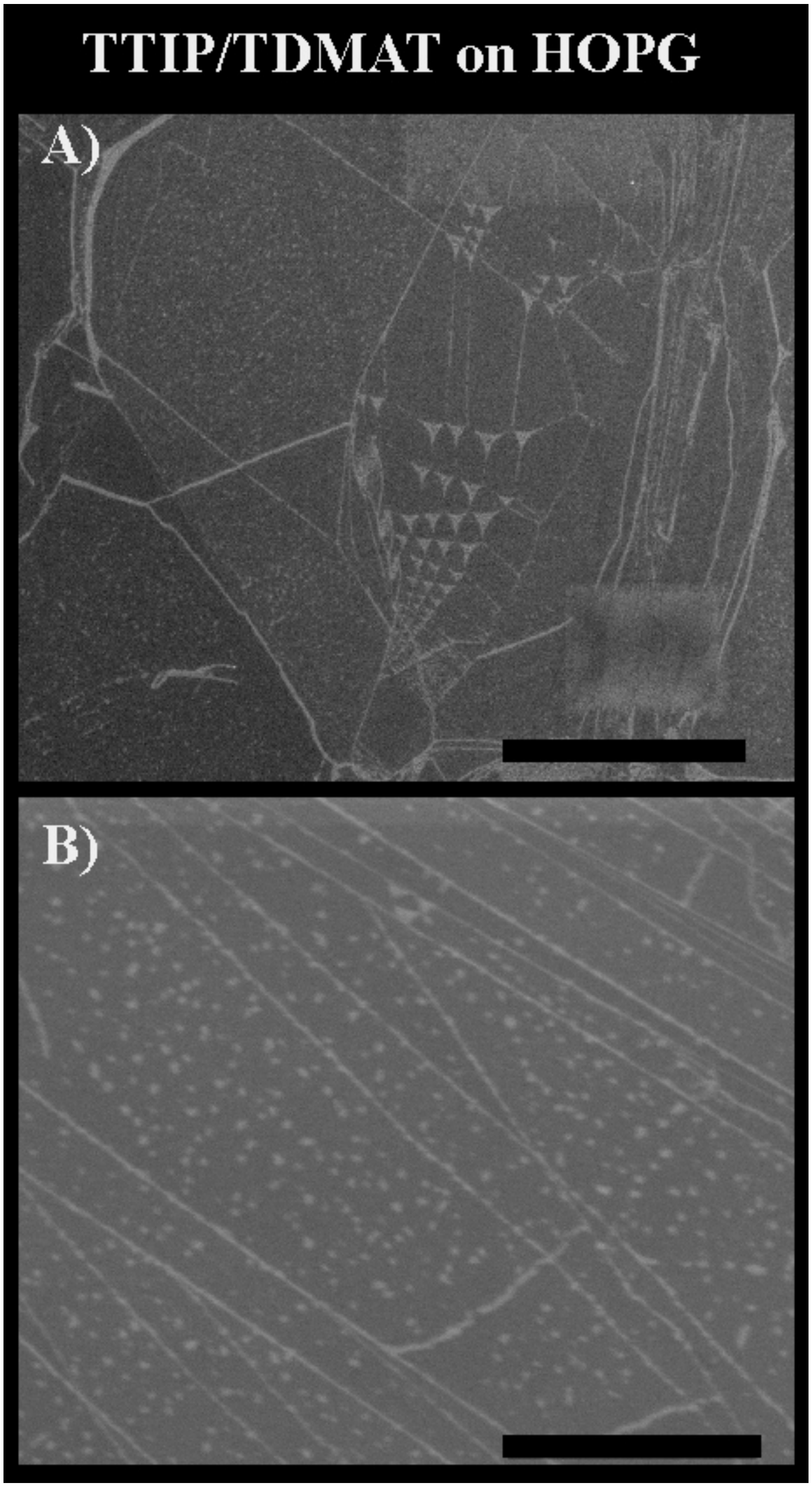

Figure 3-1. SEM images of HOPG patterned with the TTIP/TDMAT water-free recipe. A) Triangular network deposition patterns and B) Line defect patterns or step edges. Scale bars are 5 microns.

Figure 3-2 shows the results of the TTIP/TDMAT sa-ALD recipe deposited onto mechanically exfoliated few-layer graphene on gold. As with HOPG, the deposition aggregates along line defects and step edges while deposition on the basal plane is inhibited. This trend is supported by the robust film deposited on line defects with very little deposition on the basal plane. This system, however, does not result in successful selective deposition onto monolayer CVD-graphene. This water-free ALD recipe fails to result in highly anisotropic deposition of thicker films. The TiO_2 does not grow quickly on CVD-graphene and as the number of cycles increases, the metal oxide film becomes more conformal. In addition, the presence of polymer residue, folds, and tears on the graphene sheet add more nucleation sites, which amplifies the rate at which the film becomes conformal. As a result, the project shifted to more reactive mixed-metal oxide films which grow at a higher rate and have a larger temperature window to process.

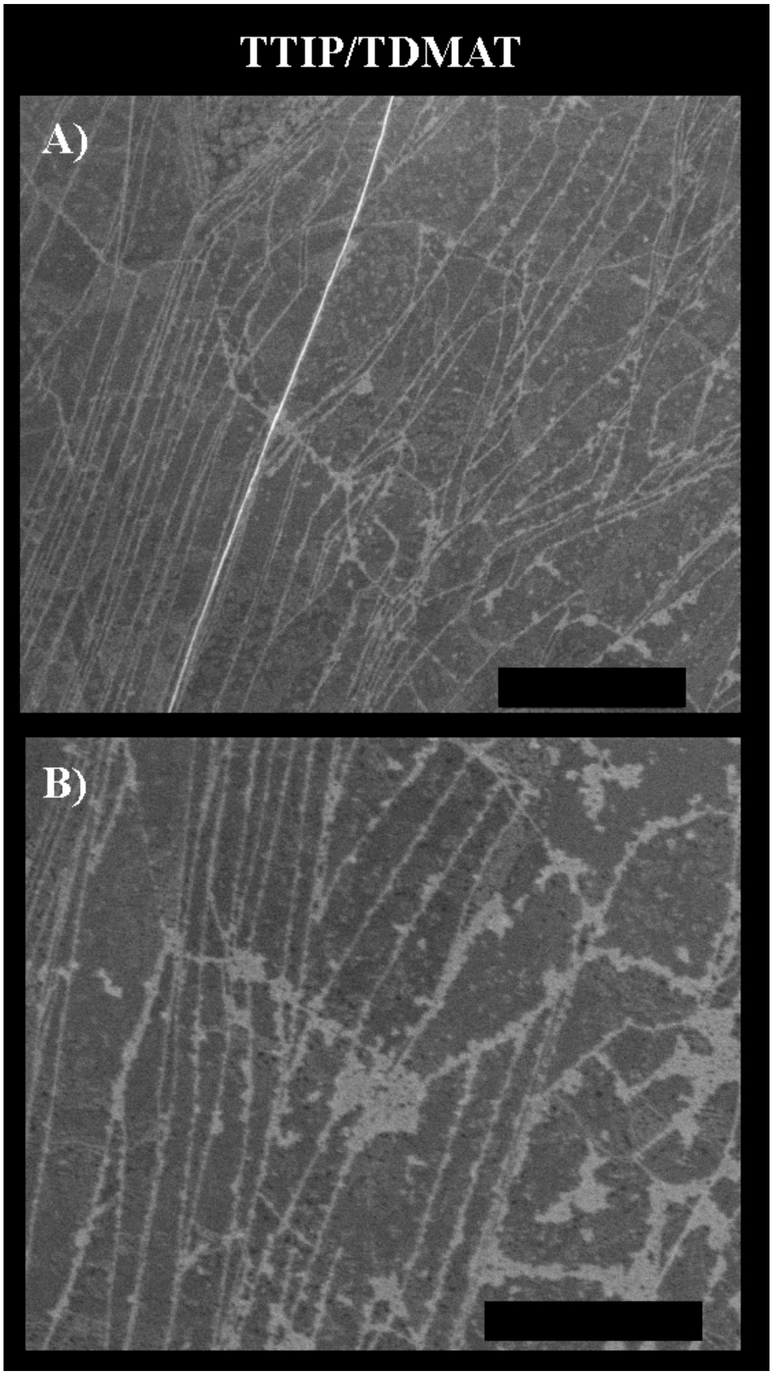

Figure 3-2. SEM images of the TTIP/TDMAT water-free recipe performed on exfoliated few-layer graphene. Scale bars 5 microns (A) and 3 microns (B).

3.4 Selective Deposition onto CVD-synthesized Graphene

Figure 3-3 shows an SEM image of the CVD-synthesized monolayer graphene on silicon after 200 cycles of the mixed-metal oxide TTIP/TMA recipe deposited at 110 ˚C. The metal-oxide was preferentially deposited in linear networks, with as-deposited regions appearing bright relative to the inert graphene sheet. Additional island deposits can be assigned to either point defects or random nucleation sites such as dust or polymer residue resulting from the wet transfer. The selective deposition chemistry occurred across wide areas on the graphene sheet (Figure 3-3b). Layered materials, as stated in Chapter 1, lack dangling bonds on the basal plane. Consequently ALD film growth occurs preferentially at step edges and defect sites.[20, 21] The sp^3-carbon or otherwise functionalized species at these grain boundaries, folds, and line defects are substantially more reactive than the pristine basal plane. When a strong oxidant is removed from the recipe, the basal plane is not supersaturated with water molecules or hydroxyl groups. The deposition chemistry therefore becomes increasingly favorable on defect sites, creating the conditions necessary for anisotropic nucleation.

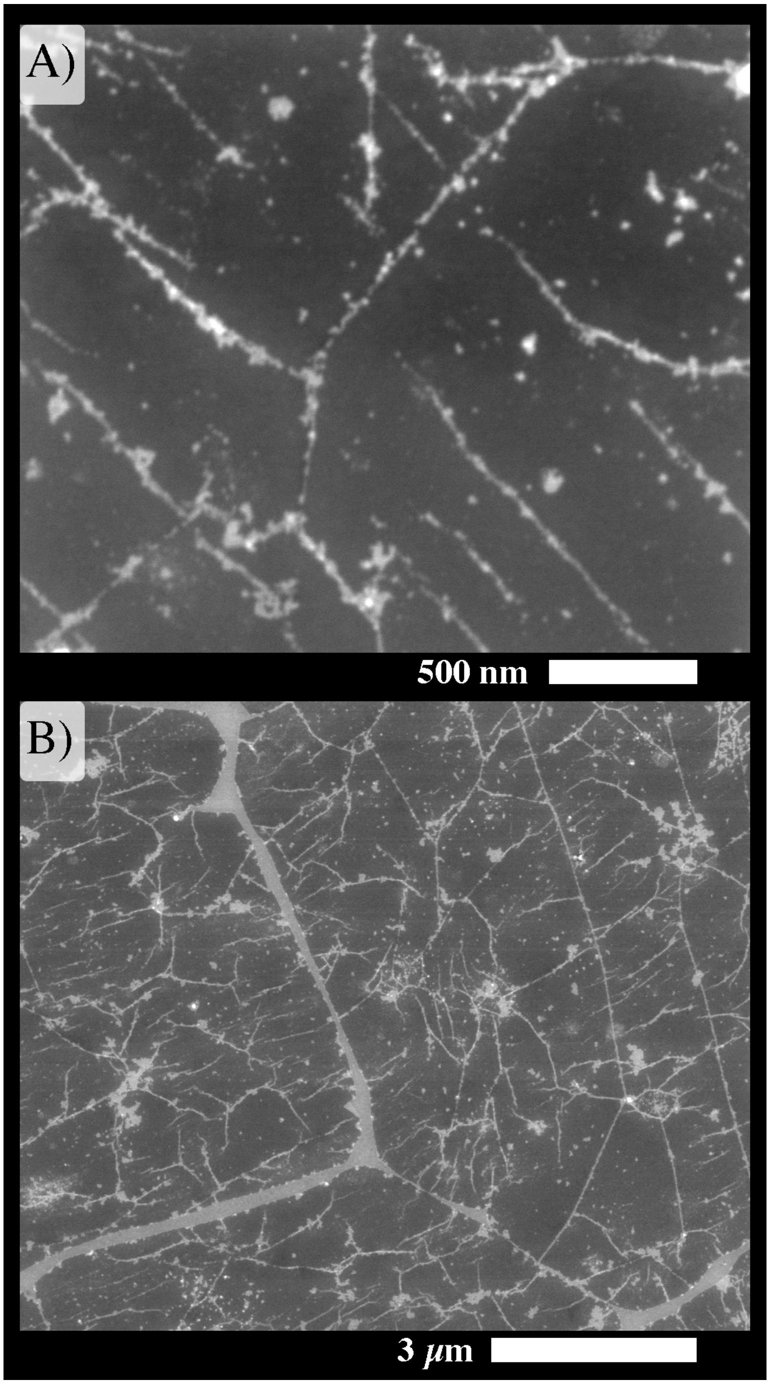

Figure 3-3. Investigation of passivated graphene sheets. A) High-resolution SEM image of a CVD-grown monolayer graphene sheet patterned with 200 cycles of the water-free ALD recipe. B) Wide-area SEM image showing point defects, line defects, and tears in the graphene sheet patterned over large areas.

Consistently, use of a water-based Al_2O_3 recipe quickly resulted in a non-conformal but isotropic film (Figure 3-4a). Line features assigned to initial defect nucleation were observed throughout the film. Little deposition was observed with only moderate selectivity for line defects in the TiO_2 water-based control (Figure 3-4b). This result is consistent with a substantially lower growth rate for TTIP relative to TMA at 110 ˚C. These control experiments indicate that removing water from the recipe directed anisotropic deposition and allowed for robust anisotropic films to form on the surface before creating a conformal film.

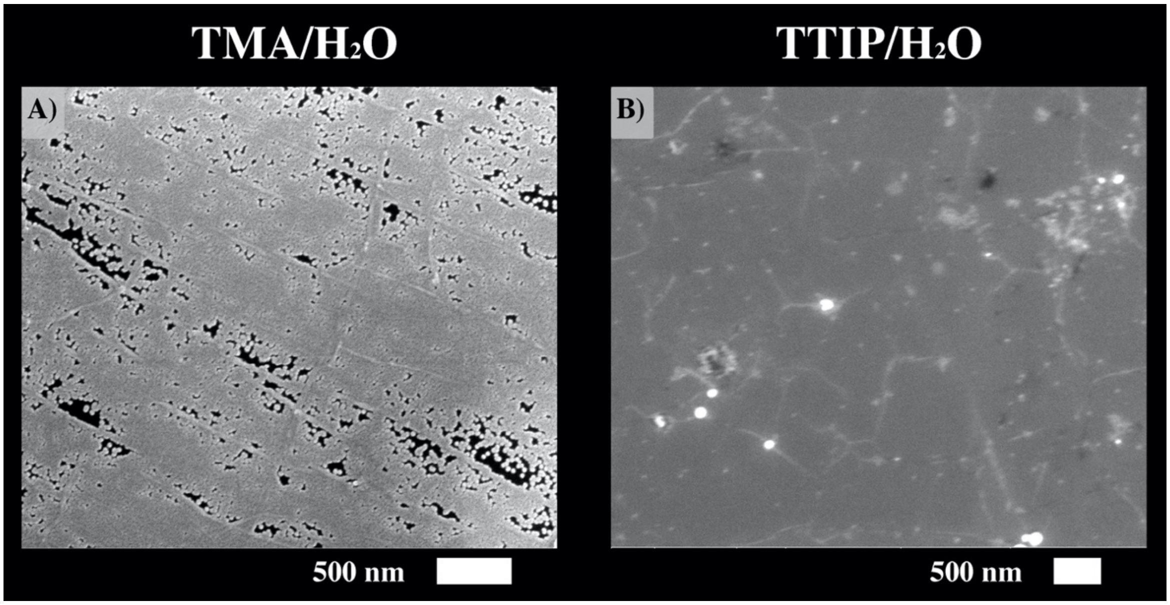

Figure 3-4. SEM images of monolayer graphene samples after 200 ALD cycles. A) Water-based aluminum oxide deposition and B) Water-based titanium dioxide deposition.

The combined TTIP/TMA recipe was performed at various temperatures to optimize the anisotropic growth behavior as well as to probe the surface chemistry (Figure 3-5). Each sample was deposited according to the recipe outlined in the materials section, and SEM data were collected after 200 cycles. The chemistry was strongly dependent on the deposition temperature. At low temperatures, selectivity was lost and the metal oxide deposition resembled a nonconformal film (Figure 3-5a). The deposition was most anisotropic at 110 ˚C, with very little deposition observed outside of the line patterns (Figure 3-5b). At higher temperatures, deposition occurred at random nucleation sites as well as at large-scale line networks (Figure 3-5c).

These results are consistent with a narrow regime in which selective-area ALD occurred. At very low temperatures, the metal-oxide condensed on the graphene basal plane. At higher temperatures, the metal-oxide precursors more readily reacted with the graphene basal plane, leading to more conformal coverage and less deposition concentrated on defects.

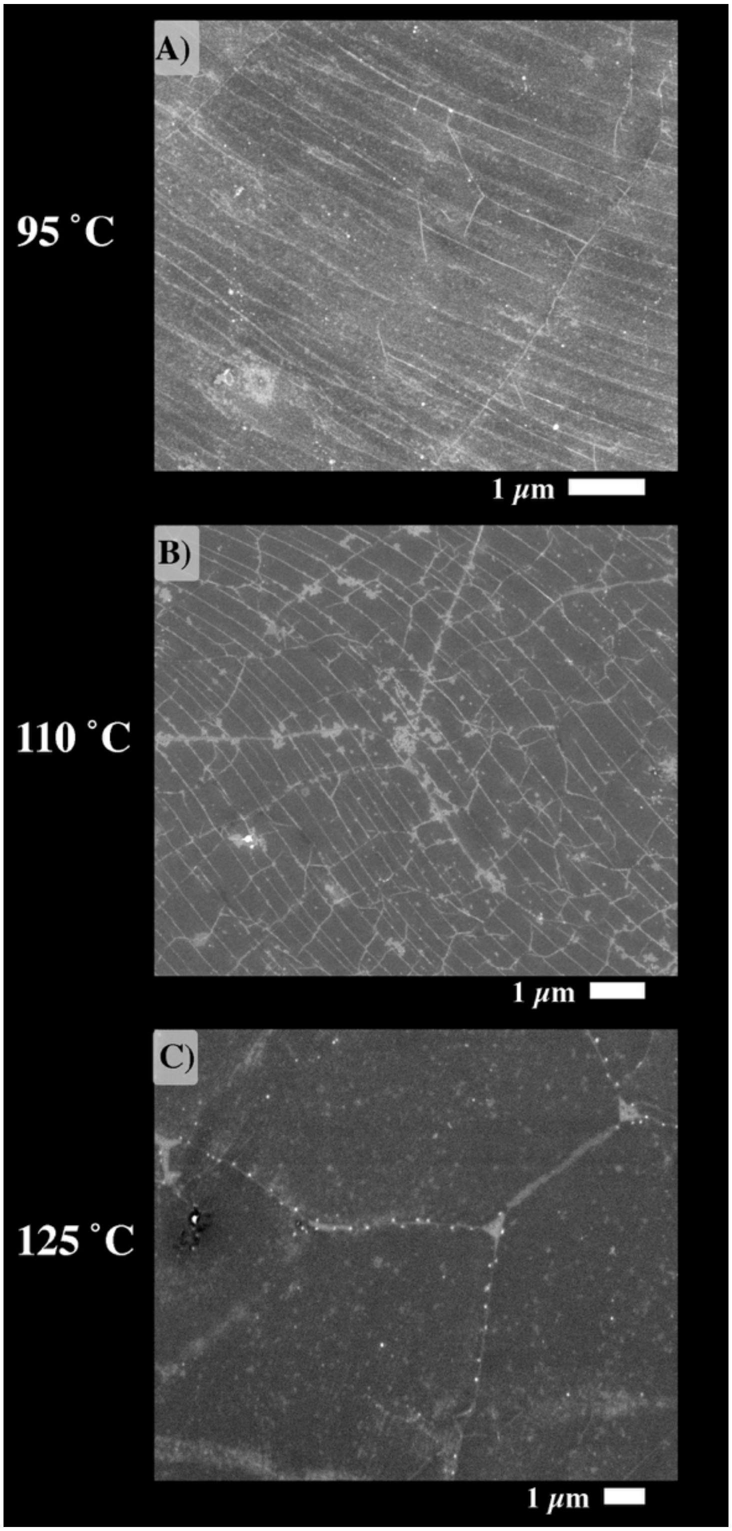

Figure 3-5. SEM images showing the temperature-dependent selectivity of the water-free ALD recipe. Images show the deposition behavior at A) 95 ˚C, B) 110 ˚C, and C) 125 ˚C.

AFM was performed in addition to SEM to evaluate the morphology and film quality after 200 ALD cycles (Figure 3-6). Significant oxide deposition occurred at line defects, with resulting films at or approaching 10 nm thick (Figure 3-6b). Using 10 nm as an upper maximum, the growth rate on defect regions on the graphene sheet was near 0.5 Å cycle^{-1}, well within the expected range based on reported growth rates of 1.33 and 0.11 Å cycle^{-1} at 110 ˚C for the water-based TMA and TTIP recipes, respectively.[22,23]

Selective-area ALD reflects a competition between intrinsic differences in substrate reactivity and the inherent self-reinforcing nucleation chemistry of island film growth.[24] The degree of selectivity in an ALD process is therefore determined by the thickness of the film in deposited regions relative to deposition on the pristine basal plane. The >10 nm thick films reported herein can be selectively deposited on defects, generating a robust passivating layer on defective regions on the graphene surface. This process can be developed further, as both the SEM data in Figure 3-3 and the AFM data in Figure 3-6 do not show the film converging into a conformal layer. KPFM mapping data were obtained concurrently with the AFM data and are shown in Figure 3-7. These maps showed clear differences in the contact potential and in the adhesion force between the line defects selectively passivated with $Al_xTi_yO_z$ and the graphene basal plane. These data were not shown with a trace because the surface scanned was not calibrated to a reference sample. However this KPFM data clearly show a patterned surface with a well-defined, non-conformal passivating layer alongside the pristine graphene surface.

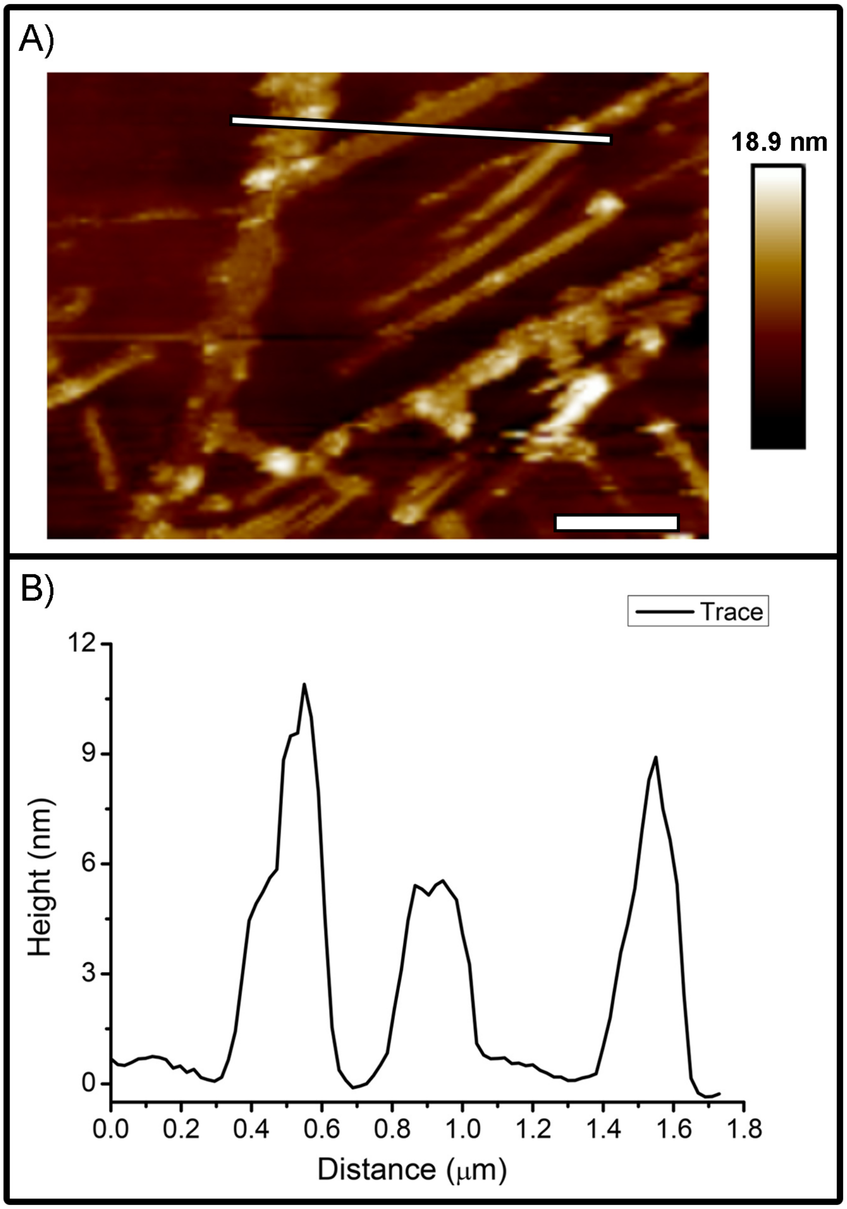

Figure 3-6 Determining film thickness. A) Atomic-force microscopy images showing selective metal oxide deposition onto line defects. Scale bar 500 nm. B) Topographic profile of the white trace in Figure 3-6a.

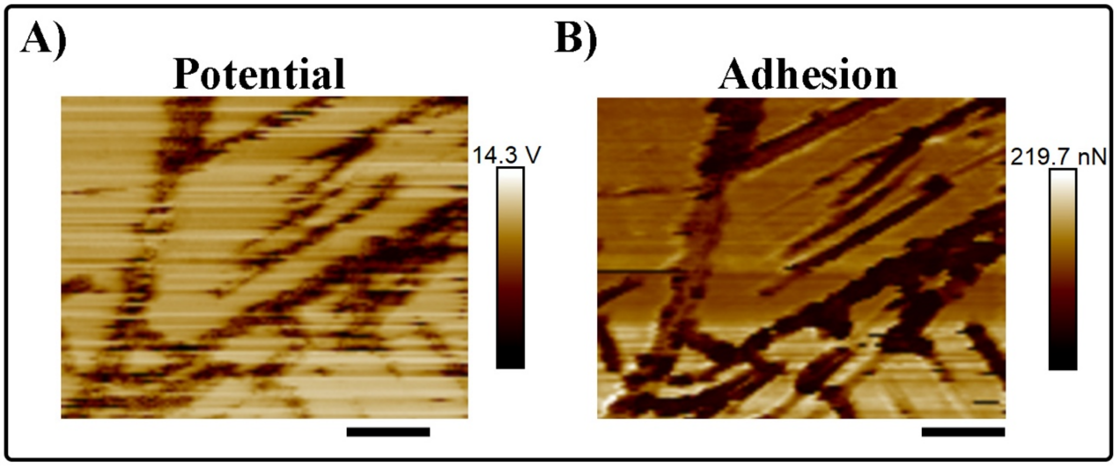

Figure 3-7. KPFM mapping data showing A) contact potential and B) surface adhesion force difference between the deposited defect regions and the pristine basal plane. Scale bars are 500 nm.

Figure 3-8 shows high-resolution X-ray photoelectron spectroscopic (XPS) data for the Ti 2p and Al 2p peaks for films produced by the water-based and water-free ALD recipes, respectively. As a reference, standard water-based ALD recipes were used to deposit Al_2O_3 and TiO_2 onto graphene films. The Ti 2p data indicate that titanium dioxide was deposited from both the water-based and water-free recipe. A small peak shift observed in the film produced by the water-free recipe (459 eV) can be attributed to the high concentration of Al^{3+} in the mixed-metal oxide film, because the more electronegative Al^{3+} metal cation will increase the relative concentration of Ti^{4+} in the film and shift the Ti 2p peak to higher binding energy.[25] The 7:1 ratio of aluminum: titanium is in good agreement with the growth rate of each precusor when reacted with water at 110 ˚C, with titanium oxide expected to grow 10 times slower than aluminum oxide. The data thus indicate that the composition of the film can be modified by adjusting the pulse times for each precursor. The TTIP/TMA pulse produced Al_2O_3 with a peak binding energy of (74.6 eV), whereas TMA/H_2O yielded alumina films with a shoulder near 73 eV and a substantially broadened full emission. This shoulder at lower binding energy is consistent with incomplete reactions and impurities in the film including incorporation of hydroxl species due to the low deposition temperature.

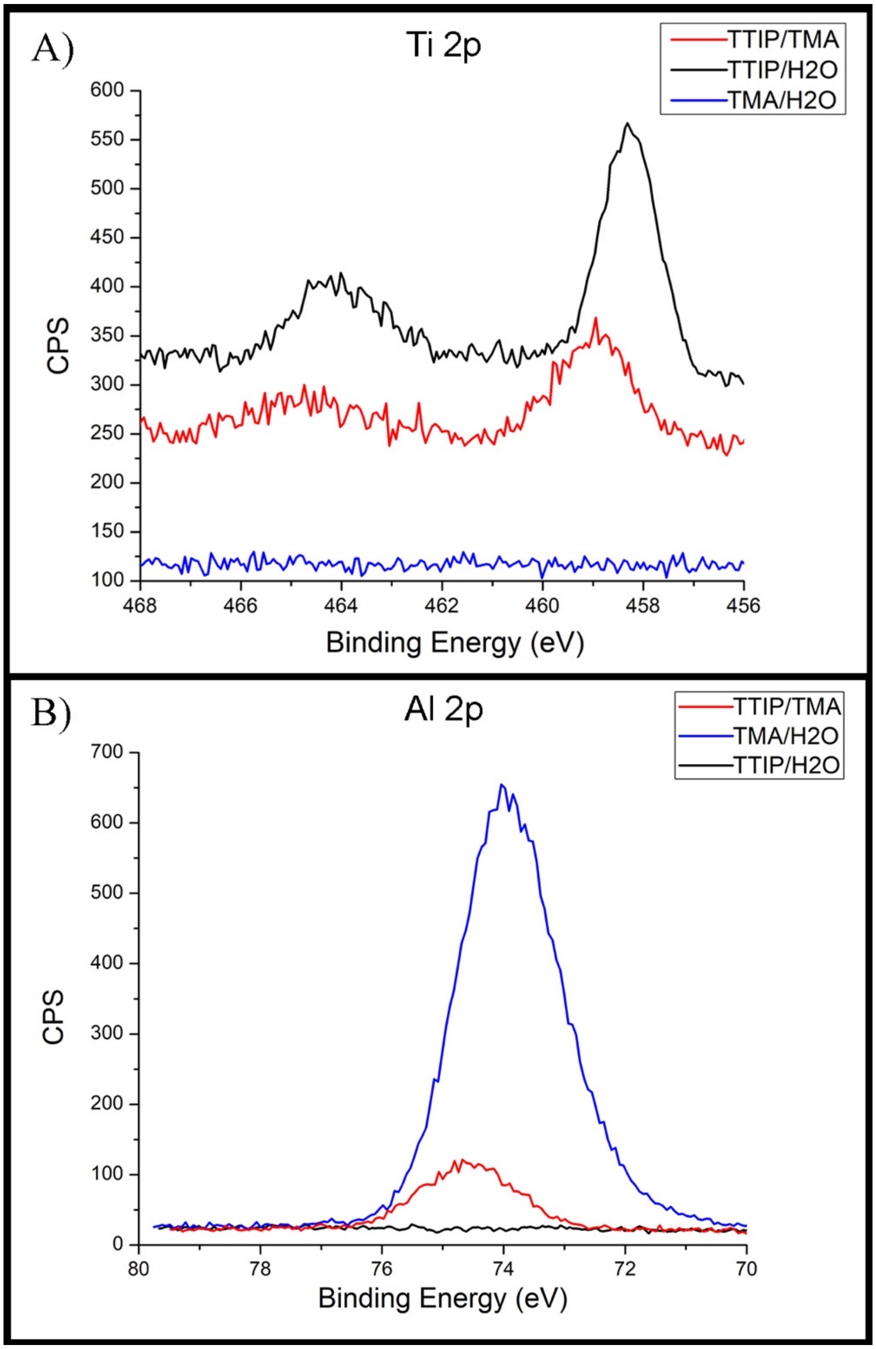

Figure 3-8. High-resolution XPS data of the as-deposited metal-oxide films on graphene. A) Titanium 2p region for both water-based controls and the water-free deposition scheme. B) Aluminum 2p region for both water-based controls and the water-free deposition scheme.

3.5 Conclusions and Future Outlook

In this chapter, sa-ALD onto graphite and graphene is achieved by developing a water-free ALD technique. This technique currently requires the TTIP precursor, as the metal-oxygen bond present in the precursor is necessary for this process. Future work will develop water-free recipes with different metal precursors, or synthesize new precursors with a metal-oxygen bond. This system can be further optimised to maximize the thickness of the passivating layer. Slight changes to the deposition temperature or increasing the purge time could further increase selectivity. Future work will be performed to determine the electronic, optical, and physical properties of the passivated layer and tune the stiochiometry of the mixed-metal oxide layer by modifying the pulse times of each precursor.

3.6 Appendix I: Defect-Selective ALD of Manganese Oxide onto HOPG

An attempt was made to selectively deposit manganese oxide onto HOPG with bis(ethylcyclopentadienyl)manganese ($(EtCp)_2Mn$ 98% STREM) as the manganese precursor and water as the counter reactant. The theory for this defect-selective mechanism involved tailoring the ligand to drive selective growth on the step edges of the HOPG substrate. The manganese precursor has a similar cyclopentadienyl structure as the platinum precursor that deposits onto line defects with excellent selectivity.[18] This system was ultimately difficult to control, as manganese oxide grows very quickly and likely nucleates at step edges first but resembles a patchy film quickly. This system was not effective, but became moderately selective with very low pulse times and very long purge times. The data is published here, as the approach of tailoring the structure of the metal organic precursor deserves research attention. As mentioned in the main text, precursors with metal-oxygen bonds are necessary for water-free ALD processes and more metal oxides can be selectively deposited by expanding the library of ALD precursors with such a bond structure. Understanding how different metal organic precursors react with target substrates will benefit the field and further our understanding of a technique that is, fundamentally, a surface chemistry process.

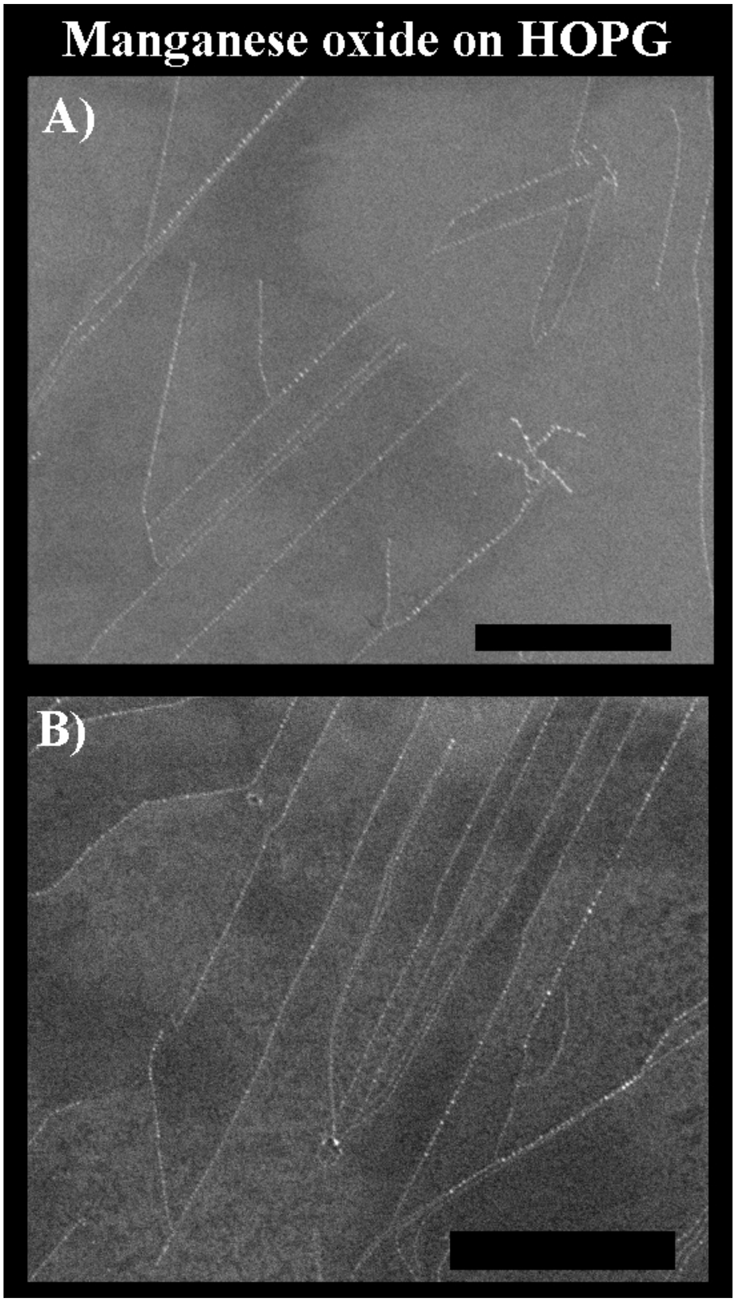

Figure S3-1. SEM images of manganese oxide deposited onto HOPG (A and B). Scale bars are 500 nm.

3.7 References

1. Novoselov, K. S.; Geim, A. K.; Morozov, S. V.; Jiang, D.; Zhang, Y.; Dubonos, S. V.; Grigorieva, I. V.; Firsov, A. A. Electric Field Effect in Atomically Thin Carbon Films. *Science* **2004**, *306* (5696), 666–669.

2. Lee, C.; Wei, X.; Kysar, J. W.; Hone, J. Measurement of the Elastic Properties and Intrinsic Strength of Monolayer Graphene. *Science* **2008**, *321* (5887), 385–388.

3. Castro Neto, A. H.; Guinea, F.; Peres, N. M. R.; Novoselov, K. S.; Geim, A. K. The Electronic Properties of Graphene. *Reviews of Modern Physics* **2009**, *81* (1), 109–162.

4. Yi, M.; Shen, Z. A Review on Mechanical Exfoliation for the Scalable Production of Graphene. *Journal of Materials Chemistry A.* **2015**, *3* (22), 11700–11715.

5. Norimatsu, W.; Kusunoki, M. Epitaxial Graphene on SiC{0001}: Advances and Perspectives. *Physical Chemistry Chemical Physics* **2014**, *16* (8), 3501–3511.

6. Bae, S.; Kim, H.; Lee, Y.; Xu, X.; Park, J.-S.; Zheng, Y.; Balakrishnan, J.; Lei, T.; Ri Kim, H.; Song, Y. I.; Kim, Y.-J.; Kim, K. S.; Özyilmaz, B.; Ahn, J.-H.; Hong, B. H.; Iijima, S. Roll-to-Roll Production of 30-Inch Graphene Films for Transparent Electrodes. *Nature Nanotechnology* **2010**, *5* (8), 574–578.

7. Yu, Q.; Jauregui, L. A.; Wu, W.; Colby, R.; Tian, J.; Su, Z.; Cao, H.; Liu, Z.; Pandey, D.; Wei, D.; Chung, T. F.; Peng, P.; Guisinger, N. P.; Stach, E. A.; Bao, J.; Pei, S.-S.; Chen, Y. P. Control and Characterization of Individual Grains and Grain Boundaries in Graphene Grown by Chemical Vapour Deposition. *Nature Materials* **2011**, *10* (6), 443–449.

8. Tian, W.; Li, W.; Yu, W.; Liu, X. A Review on Lattice Defects in Graphene: Types, Generation, Effects and Regulation. *Micromachines (Basel)* **2017**, *8* (5), 163.

9. Fan, X.; Wagner, S.; Schädlich, P.; Speck, F.; Kataria, S.; Haraldsson, T.; Seyller, T.; Lemme, M. C.; Niklaus, F. Direct Observation of Grain Boundaries in Graphene through Vapor Hydrofluoric Acid (VHF) Exposure. *Science Advances* **2018**, *4* (5), eaar5170.

10. Johnson, R. W.; Hultqvist, A.; Bent, S. F. A Brief Review of Atomic Layer Deposition: From Fundamentals to Applications. *Materials Today* **2014**, *17* (5), 236–246.

11. Hagen, D. J.; Pemble, M. E.; Karppinen, M. Atomic Layer Deposition of Metals: Precursors and Film Growth. *Applied Physics Reviews* **2019**, *6* (4), 041309.

12. Merkx, M. J. M.; Vlaanderen, S.; Faraz, T.; Verheijen, M. A.; Kessels, W. M. M.; Mackus, A. J. M. Area-Selective Atomic Layer Deposition of TiN Using Aromatic

Inhibitor Molecules for Metal/Dielectric Selectivity. *Chemistry of Materials* **2020**, *32* (18), 7788–7795.

13. Mackus, A. J. M.; Merkx, M. J. M.; Kessels, W. M. M. From the Bottom-Up: Toward Area-Selective Atomic Layer Deposition with High Selectivity. *Chemistry of Materials* **2019**, *31* (1), 2–12.

14. Cao, K.; Cai, J.; Liu, X.; Chen, R. Review Article: Catalysts Design and Synthesis via Selective Atomic Layer Deposition. *Journal of Vacuum Science & Technology A* **2018**, *36* (1), 010801.

15. Hashemi, F. S. M.; Bent, S. F. Sequential Regeneration of Self-Assembled Monolayers for Highly Selective Atomic Layer Deposition. *Advanced Materials & Interfaces* **2016**, *3* (21), 1600464.

16. Atanasov, S. E.; Kalanyan, B.; Parsons, G. N. Inherent Substrate-Dependent Growth Initiation and Selective-Area Atomic Layer Deposition of TiO_2 Using "Water-Free" Metal-Halide/Metal Alkoxide Reactants. *Journal of Vacuum Science & Technology A* **2016**, *34* (1), 01A148.

17. Singh, J. A.; Thissen, N. F. W.; Kim, W.-H.; Johnson, H.; Kessels, W. M. M.; Bol, A. A.; Bent, S. F.; Mackus, A. J. M. Area-Selective Atomic Layer Deposition of Metal Oxides on Noble Metals through Catalytic Oxygen Activation. *Chemistry of Materials* **2018**, *30* (3), 663–670.

18. Kim, K.; Lee, H.-B.-R.; Johnson, R. W.; Tanskanen, J. T.; Liu, N.; Kim, M.-G.; Pang, C.; Ahn, C.; Bent, S. F.; Bao, Z. Selective Metal Deposition at Graphene Line Defects by Atomic Layer Deposition. *Nat Communications* **2014**, *5* (1), 4781.

19. Lee, H.-B.-R.; Baeck, S. H.; Jaramillo, T. F.; Bent, S. F. Growth of Pt Nanowires by Atomic Layer Deposition on Highly Ordered Pyrolytic Graphite. *Nano Letters* **2013**, *13* (2), 457–463.

20. Wang, X.; Tabakman, S. M.; Dai, H. Atomic Layer Deposition of Metal Oxides on Pristine and Functionalized Graphene. *Journal of the American Chemical Society.* **2008**, *130* (26), 8152–8153.

21. Mazza, M. F.; Cabán-Acevedo, M.; Wiensch, J. D.; Thompson, A. C.; Lewis, N. S. Defect-Seeded Atomic Layer Deposition of Metal Oxides on the Basal Plane of 2D Layered Materials. *Nano Letters* **2020**, *20* (4), 2632–2638.

22. Groner, M. D.; Fabreguette, F. H.; Elam, J. W.; George, S. M. Low-Temperature Al_2O_3 Atomic Layer Deposition. *Chemistry of Materials* **2004**, *16* (4), 639–645.

23. Xie, Q.; Jiang, Y.-L.; Detavernier, C.; Deduytsche, D.; Van Meirhaeghe, R. L.; Ru, G.-P.; Li, B.-Z.; Qu, X.-P. Atomic Layer Deposition of TiO2 from Tetrakis-Dimethyl-

Amido Titanium or Ti Isopropoxide Precursors and H2O. *Journal of Applied Physics* **2007**, *102* (8), 083521.

24. Puurunen, R. L.; Vandervorst, W.; Besling, W. F. A.; Richard, O.; Bender, H.; Conard, T.; Zhao, C.; Delabie, A.; Caymax, M.; De Gendt, S.; Heyns, M.; Viitanen, M. M.; de Ridder, M.; Brongersma, H. H.; Tamminga, Y.; Dao, T.; de Win, T.; Verheijen, M.; Kaiser, M.; Tuominen, M. Island Growth in the Atomic Layer Deposition of Zirconium Oxide and Aluminum Oxide on Hydrogen-Terminated Silicon: Growth Mode Modeling and Transmission Electron Microscopy. *Journal of Applied Physics* **2004**, *96* (9), 4878–4889.

25. Lu, Y.; Xie, X.; Fang, W. Insight into the Property Modification of Zr-Incorporated Alumina Binary Mixed Oxides by XRD, TEM, XPS, TPD and IR. *Chemistry Select* **2020**, *5* (26), 7928–7933. https://doi.org/10.1002/slct.202001635.